Lappeenranta University of Technology
LUT School of Engineering Science
Master's Programme in Computational Engineering and Physics

Svetlana Tcvetkova

ARTIFICIAL REFLECTING STRUCTURES BASED ON METAMATERIALS

Examiner: Professor Erkki Lähderanta

ABSTRACT

Lappeenranta University of Technology
LUT School of Engineering Science
Master's Programme in Computational Engineering and Physics

Svetlana Tcvetkova

Artificial reflecting structures based on metamaterials

Master's Thesis
2015

43 pages, 27 figures, 4 table, and 3 appendices.

Examiner: Professor Erkki Lähderanta

Keywords: focusing metamirror, Huygens' surface, angular stability, reflecting metasurface

This thesis studies metamaterial-inspired mirrors which provide the most general control over the amplitude and phase of the reflected wavefront. The goal is to explore practical possibilities in designing fully reflective electromagnetic structures with full control over reflection phase. The first part of the thesis describes a planar focusing metamirror with the focal distance less than the operating wavelength. Its practical applicability from the viewpoint of aberrations when the incident angle deviates from the normal one is verified numerically and experimentally. The results indicate that the proposed focusing metamirror can be efficiently employed in many different applications due to its advantages over other conventional mirrors. In the second part of the thesis a new theoretical concept of reflecting metasurface operation is introduced based on Huygens' principle. This concept in contrast to known approaches takes into account all the requirements of perfect metamirror operation. The theory shows a route to improve the previously proposed metamirrors through tilting the individual inclusions of the structure at a chosen angle from normal. It is numerically tested and the results demonstrate improvements over the previous design.

Acknowledgments

This thesis was made in Aalto University School of Electrical Engineering at the Department of Radio Science and Engineering in the research group of Theoretical and Applied Electromagnetics of Complex Media in 2015. I would like to thank my supervisor Professor Sergei Tretyakov for giving me a chance to work in this research group, support, motivation and inspiration during the difficulties. I am also grateful to my instructor M.Sc. Viktar Asadchy for the assistance throughout my thesis work and sharing his knowledge with me. I want to wish all the best to the members of RAD department (Aalto University) for the warm atmosphere.

I am thankful to Professor Erkki Lähderanta for a possibility to study in Lappeenranta University of Technology and support of my choice in the thesis research area.

I am much obliged to my mentor Evgeny Svechnikov for believing in me and my abilities.

Finally, I would like to thank my dear family and friends who have never doubted in me and supported me during the studies.

Otaniemi, 20.5.2015

Svetlana Tcvetkova

Contents

Symbols

A	Positive constant in the parabola equation
$\boldsymbol{B}$	Magnetic flux density
b	Width of an incident beam
C	Depth of reflector
c	Width of a reflected beam
$\boldsymbol{D}$	Electric flux density
d	Distance between focal spot at normal incidence and at oblique incidence
D	Diameter of reflector
$\boldsymbol{E}$	Electric field vector
$\boldsymbol{E}_{\mathrm{inc}}$	Incident electric field vector
$\boldsymbol{E}_{\mathrm{ref}}$	Reflected electric field vector
$\boldsymbol{E}_{\mathrm{t}}$	Transmitted electric field vector
E_{inc}	Incident electric field amplitude
f	Frequency
F	Focal length
$\boldsymbol{H}$	Magnetic field vector
$\boldsymbol{H}_{\mathrm{inc}}$	Incident magnetic field vector
$\boldsymbol{H}_{\mathrm{ref}}$	Reflected magnetic field vector
$\boldsymbol{H}_{\mathrm{t}}$	Transmitted electric field vector
H_{inc}	Incident magnetic field amplitude
$\boldsymbol{J}_{\mathrm{e}}$	Electric current density
$\boldsymbol{J}_{\mathrm{m}}$	Magnetic current density
$\boldsymbol{J}_{\mathrm{se}}$	Surface electric current density
$\boldsymbol{J}_{\mathrm{sm}}$	Surface magnetic current density
$\boldsymbol{k}_{\mathrm{inc}}$	Wave vector of an incident wave
$\boldsymbol{k}_{\mathrm{ref}}$	Wave vector of an reflected wave
k_0	Wavenumber of free space
l	Length of metal wire
$\boldsymbol{m}$	Magnetic dipole moment vector
$\boldsymbol{n}$	Normal
$\boldsymbol{p}$	Electric dipole moment vector
r_0	Wire radius
S	Area of the unit cell
S_{21}	Transmission coefficient of a two-port network
ε_0	Permittivity of free space

ε	Relative permittivity
$\overline{\overline{\hat{\alpha}}}_{\mathrm{ee}}$	Effective electric polarizability dyadic
$\overline{\overline{\hat{\alpha}}}_{\mathrm{em}}$	Effective electro-magnetic polarizability dyadic
$\overline{\overline{\hat{\alpha}}}_{\mathrm{me}}$	Effective magneto-electric polarizability dyadic
$\overline{\overline{\hat{\alpha}}}_{\mathrm{mm}}$	Effective magnetic polarizability dyadic
$\overline{\overline{\alpha}}_{\mathrm{ee}}$	Individual electric polarizability dyadic
$\overline{\overline{\alpha}}_{\mathrm{em}}$	Individual electro-magnetic polarizability dyadic
$\overline{\overline{\alpha}}_{\mathrm{me}}$	Individual magneto-electric polarizability dyadic
$\overline{\overline{\alpha}}_{\mathrm{mm}}$	Individual magnetic polarizability dyadic
β_{e}	Electric-field interaction constant
β_{m}	Magnetic-field interaction constant
η	Wave impedance
η_0	Wave impedance of free space
θ	Angle between normal and reflected wave vector
θ_{b}	Beam deflection angle
θ_{F}	Focus deflection angle
ρ_{e}	Electric charge density
ρ_{m}	Magnetic charge density
ρ_{se}	Surface electric charge density
ρ_{sm}	Surface magnetic charge density
κ	Strength of chirality
λ	Wavelength
μ_0	Permeability of free space
μ	Relative permeability
ϕ	Desired phase
ϕ_0	Phase at the $y = 0$ point
ω	Angular frequency
Ω	Omega-coupling coefficient

Abbreviations and Acronyms

cm	Centimetre
GHz	GigaHertz
HFSS	High Frequency Structure Simulator
mm	Millimetre
PEC	Perfect Electric Conductor
PMC	Perfect Magnetic Conductor
RF	Radio Frequency
SRR	Split Ring Resonator
TEM	Transverse Electromagnetic

List of Figures and Tables

List of Figures

List of Tables

1 Introduction

Metamaterial is an arrangement of artificial structural elements, designed to achieve advantageous and unusual electromagnetic properties [1]. All the electromagnetic characteristics of these man-made materials depend primarily on their internal structure, in contrast to natural materials whose properties are defined mostly by their chemical composition. Therefore, adjusting the structure of metamaterials and their constituent elements, so-called "meta-atoms", one can achieve novel properties, functionalities and, thus, new possibilities for applications. The size of the construction elements must be much smaller compared to the wavelength at which they operate. This condition implies that the artificial composite can be modelled as an effectively homogeneous medium.

One can distinguish three original classes of metamaterials that have been intensively developed [2]. The first kind appeared in a theoretical description written by prof. Victor Veselago in 1967: this is so-called left-handed material (LHM) or negative-index materials (NIM) [3, 4]. These substances have negative permittivity and permeability and, as a result, negative refractive index. Negative refraction takes place at an interface with a usual isotropic material, in reverse to the usual refraction phenomenon (Figure 1). The phase velocity vector in left-handed materials is anti-parallel to the direction of the Poynting vector.

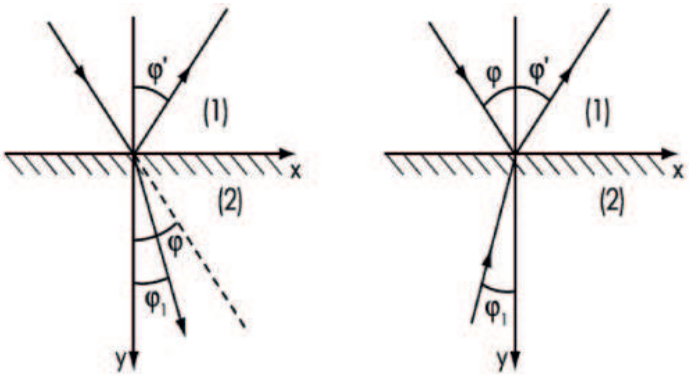

(a) (b)

Figure 1. An illustration of negative beam refraction by prof. Leonid Mandelshtam. (a) In a usual medium. (b) In a medium, where the phase velocity is negative.

Consequently, prof. David R. Smith *et al.* demonstrated the first realization of NIM at microwaves [5] (see Figure 2). Their structure consisted of straight metallic wires and split-ring resonators (SRR) which are responsible for the effective negative permittivity and negative permeability, respectively.

Figure 2. An illustration of the first NIM metamaterial construction.

Composite materials possessing artificial magnetism form the second class of metamaterials. Such materials provide a possibility to achieve the values of the effective permeability not obtainable in natural materials, in particular, a negative real component of the effective permeability [6]. A composite consisted of split-ring resonators and introduced by prof. John Pendry *et al.* in 1999 was the first metamaterial structure possessing artificial magnetism [7].

The third class of metamaterials is bianisotropic materials which include simultaneously electric and magnetic anisotropy as well as magnetoelectric coupling [8]. The bianisotropy properties can be described through the material parameters: permittivity ε, permeability μ, and the field coupling coefficients, such as the chirality parameter κ and the omega-coupling coefficient Ω. One of the most explored artificial bianisotropic materials is of the chiral type. In such a material two circularly polarized waves can propagate in each direction, having different propagation constant. The wave impedance of chiral materials does not depend on κ and it is equal to $\eta = \sqrt{\mu\mu_0/(\varepsilon\varepsilon_0)}$. Using chiral materials, it is possible to construct left-handed materials. The wave impedance of eigenwaves in omega-type bianisotropic materials is asymmetric with respect to the propagation direction reversal. Using omega materials, one can construct a layer which simultaneously operates as a perfect electric conductor (PEC) from one side and as a perfect magnetic conductor (PMC) from the other side. Another advantage of omega media is a possibility to manipulate the impedance value within a wide range.

An important issue is the dimensionality and fabrication features of metamaterials. Three-dimensional (volumetric) metamaterials which usually consist of several layers are usually rather lossy and difficult to manufacture. A metasurface is a two-dimensional (a single layer of meta-atoms) material which is not so lossy and cheaper to manufacture. Metamaterials can be used for a great variety of applications such as improvement of antenna performance,

construction of electromagnetic radiation absorbers, replacement of conventional mirrors and lenses by metamaterial reflectors and transmitters, realisation of an invisibility cloak, *et cetera*.

The goal of this thesis is to explore practical possibilities in designing fully reflective electromagnetic structures with full control over reflection phase. In particular, we focus on the case of novel metamaterial-inspired mirrors (so-called *metamirrors*) which provide the most general control over the amplitude and phase of the reflected wavefront. The work consists of two main parts. The first part describes a recently proposed [9] planar focusing metamirror with the focal distance less than the operating wavelength λ, what makes this structure unique. Previously, only focusing of the normally-incident plane waves have been studied. It could be expected that practical applicability of such a structure can be its limited angular stability (aberrations when the incidence angle deviates from the ideal one). In this thesis, the angular stability of the recently introduced focusing metamirror is tested numerically and experimentally. The results show that the proposed metamirrors are angularly stable and the focus does not degrade within a considered angle range, which is a remarkable feature in comparison with other conventional structures.

In the second part of the thesis metamirrors reflecting incident plane waves at an arbitrary angle are considered. A new theoretical concept of reflecting metasurface operation is introduced based on Huygens' principle. The description clearly explains and proves the main idea. The theory shows a route to improve the previously proposed metamirrors through tilting the individual inclusions of the structure at a chosen angle from the normal. This idea is tested numerically. The results demonstrate noticeable improvement over the previously proposed design.

The thesis is organized as following. In Section 2 the known types of reflectors are briefly discussed. Specifically, benefits and drawbacks of conventional mirrors and reflectarrays as well as novel metamirrors are described. A specific metamirror constructed with copper inclusions is considered in Section 3. It is proved numerically and experimentally that the metamirrors do not lose the operational capability under considerable deflections of incident waves from the normal and, thus, they are perfectly suitable for practical applications. Section 4 introduces a new concept of metamirrors which is described through Huygens' principle. The theoretical results described here form a foundation for further work in this direction. One of the possible ways to implement the theory is proposed and numerically tested in Section 5. Finally, Section 6 concludes the thesis and suggests ideas for future developments.

2 Reflectors

Since the ancient time the properties of mirrors have been studied. Through the use of geometric and physical properties, reflection with a certain amplitude at an arbitrary angle can be achieved. It is possible to use usual polished pieces of metal to reflect light, but since that time many things have changed. Nowadays, there are different methods to realize and control reflection of electromagnetic waves. This section presents an overview of different methods of designing reflectors, including methods based on metamaterials. The advantages and drawbacks of each approach are considered in some detail. The properties, structure and practical applications of conventional reflectarrays and parabolic antennas as well as novel artificial mirrors based on metamaterials are studied extensively. The present study is devoted to the analysis and comparison of different properties of all these methods, in particular the angular stability of the reflectors operation.

The most common application of the reflecting mirrors is focusing electromagnetic wave beams. Therefore, the parameters that determine the mirror properties are important to notice. The size of the reflecting structure should be taken in consideration because it impacts on the focusing ability as well as fabrication and maintenance. It means that smaller constructions are preferable. A short focal length allows higher energy gains in the focal spot. Combining these two characteristics, the f-number can be defined as the ratio of the focal length F and the aperture diameter D: $f = F/D$. The smaller f-number, the more electromagnetic wave power can be gathered. Thus, it provides a brighter image. To find the best focusing structure for a particular device, these remarks should be taken into account.

2.1 Parabolic and spherical reflectors

To focus the electromagnetic wave in the same plane with an incident wave, parabolic and spherical shapes of reflectors are appropriate (Figure 3). These types of mirrors are used to collect energy from a distant source and direct it to the focal point. Due to reciprocity, parabolic reflectors can be used also to direct the energy of a source located in the focal point into a parallel-ray beam. The main advantage of such reflectors is the high directivity. To produce a beam with a very narrow width the reflectors should be much larger than the wavelength of the radiated wave. This condition imposes the limitation to the possible wavelengths that can be used (for example, [10]).

The focal lengths of spherical and parabolic antennas depend on their sizes. For the former

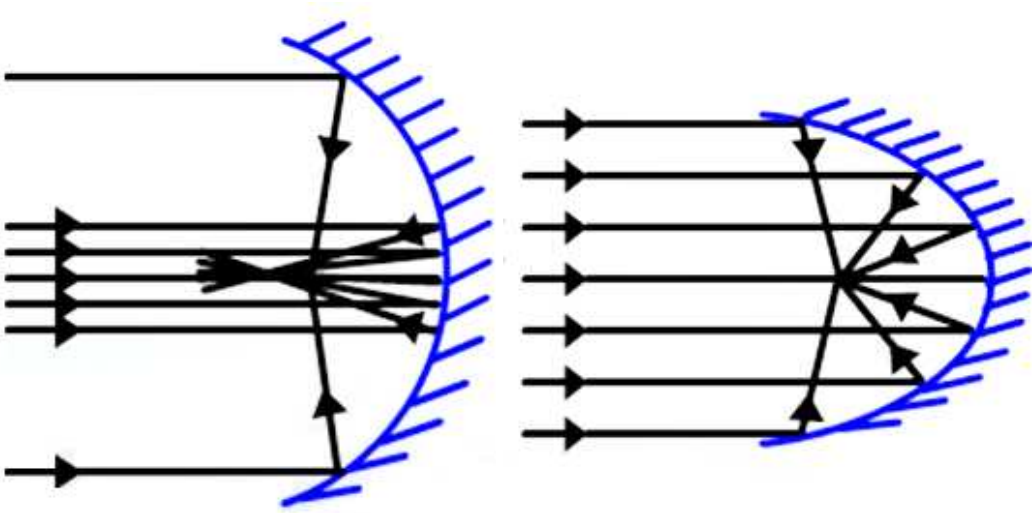

(a) (b)

Figure 3. Two types of reflectors. (a) Spherical mirror. (b) Parabolic mirror.

the focal distance F is approximately defined by the equation:

$$F \simeq \frac{1}{2} r, \tag{1}$$

and for the latter:

$$F = \frac{D^2}{16\,C}, \tag{2}$$

where r is the radius of the sphere, D is the aperture diameter and C is the depth of the reflector. For a spherical reflector to achieve a small focal length, smaller radii of the aperture are required. For a parabolic reflector, as well, the distance to the focus depends on the size of the structure. This causes limitations in applications, which are unavoidable disadvantages of conventional mirrors.

Another important characteristic of focusing mirrors is the angular stability. If the structure is not stable with respect to deviations of the the incident beam direction, it is not possible to use it in practice. As it is known, for parabolic and spherical reflectors the angles of the focal spot inclination and the incident wave deviation are roughly equal for the small angles. The case of the oblique incidence at 5 degrees is represented in Figure 4. The focal point deviates for both reflectors by nearly 6 degrees, but for the paraboloid comatic aberrations take place. For the parabolic reflector there is an approximate equation for the focus deflected angle

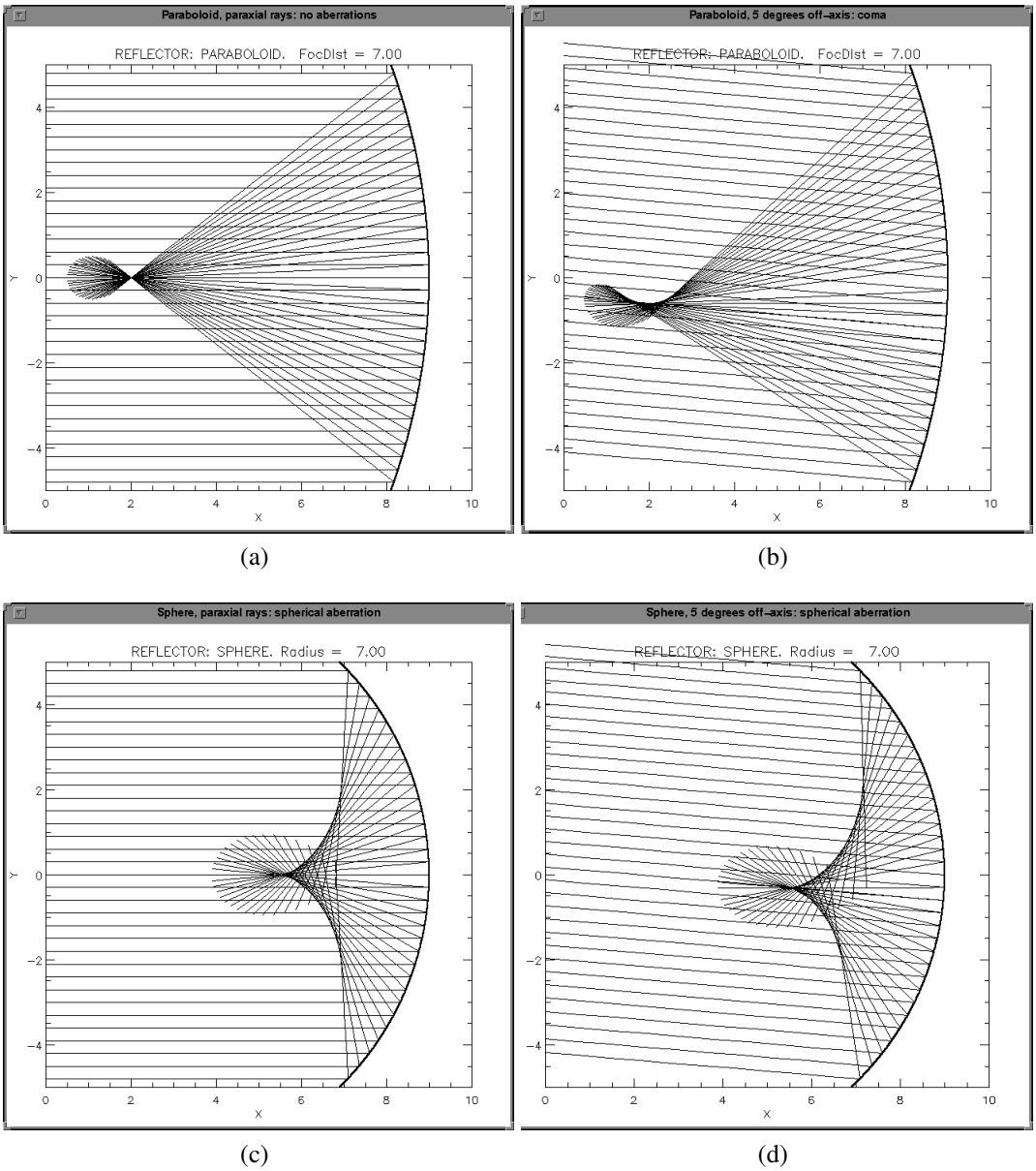

(a) (b)

(c) (d)

Figure 4. Angular stability of parabolic and spherical reflectors: (a), (c) under the normal incidence and (b), (d) under the oblique incidence (5 degree), correspondingly.

θ_{F} [11]:

$$\theta_{\mathrm{F}} \simeq \arctan \frac{\sin \theta_{\mathrm{b}}}{1 - \frac{2}{3}\left(\frac{D}{4F}\right)^2}, \tag{3}$$

where θ_{b} is the beam deflection angle and D is the maximum diameter (aperture) of the parabola.

2.2 Reflectarrays

Advantages of the reflectors and antenna arrays are combined in reflectarrays (Figure 5) [12]. For microwave applications their basic form represents an array of metal patches over a metal

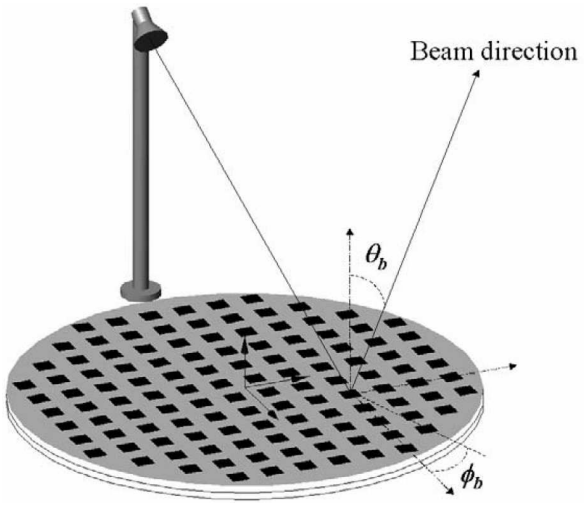

Figure 5. An illustration of a reflectarray antenna.

ground plane. All the patches usually have the same shape but their dimensions are slightly varied [13, 14]. To achieve the desired phase shift, such structures as printed patches with attached or aperture-coupled delay lines, varying-sized patches in single and stacked configurations, apertures of different length on a ground plane are utilized [15]. The benefits of reflectarrays over usual shaped metal reflectors are simplicity, low loss of the power distribution and smaller cost and mass of a printed structure. Compared with large aperture and curved-shape conventional reflectors, reflectarrays can be easier to manufacture and deploy. The reflectarray concept is not new, and the physical and commercial benefits of reflectarrays have led to different uses of these structures with a multiple variety of configurations. It should be noted that the reflectarrays can have smaller focal length comparing with the parabolic reflectors. However, in contrast to metamirrors, considered in this thesis, the dis-

tance to the focus is larger than several operating wavelengths λ. Clearly, it is advantageous to use smaller and cheaper systems than conventional mirrors.

The main limitations of reflectarrays are their narrow bandwidth and forbidden transmission at all frequencies due to the presence of the ground plane [16]. To the best of our knowledge, the angular stability of reflectarrays has not been explored in the literature.

2.3 Metamirrors

Metasurfaces are single-layer planar metamaterials which have deeply sub-wavelength thickness. The ability to manipulate the reflected and transmitted wavefronts has been demonstrated by engineering electromagnetic properties of such structures. The physical phenomena behind the wavefront control in transmission and reflection are fundamentally different. The manipulation of transmission wavefront can be performed by an array of zero backward scattering inclusions which scatter waves with the desired phase only in the forward direction. To manipulate the reflection wavefront, the elements in the array should accomplish a double task: scatter waves in the forward direction with the phase opposite to the phase of the incidence and re-radiate waves in the backward direction with a specific phase distribution [17].

Metasurfaces for tailoring wavefronts in transmission are penetrable aside from the operating frequency range, while most known metasurfaces for the manipulation of reflection are metal-backed and, therefore, imperceptible at the whole frequency spectrum. Recently, reflecting structures with the possibility of full phase control in reflection and without a ground plane were discovered. One of the potential metamirrors represents a multi-layer electrically thick composite [18]. Another one is an ultra-thin engineered structure that can provide full control of the reflected wavefronts independently from the both sides of the mirror [13]. Through the absence of a ground plane and extremely small dimensions of the elements, these metamirrors are practically transparent outside of the operational frequency band. Here we study metamirrors formed by single planar arrays of particularly shaped resonant bianisotropic inclusions (Figure 6).

There are many advantages of metamirrors. First of all, the focal length of such structures can be extremely short, a fraction of the wavelength. It can allow to gather more energy and provide a brighter image in a very compact structure. Penetrability outside of the operating frequency band is another significant benefit, compared with conventional mirrors and reflectarrays. The small size and low profile simplify deployment of reflecting metasurfaces,

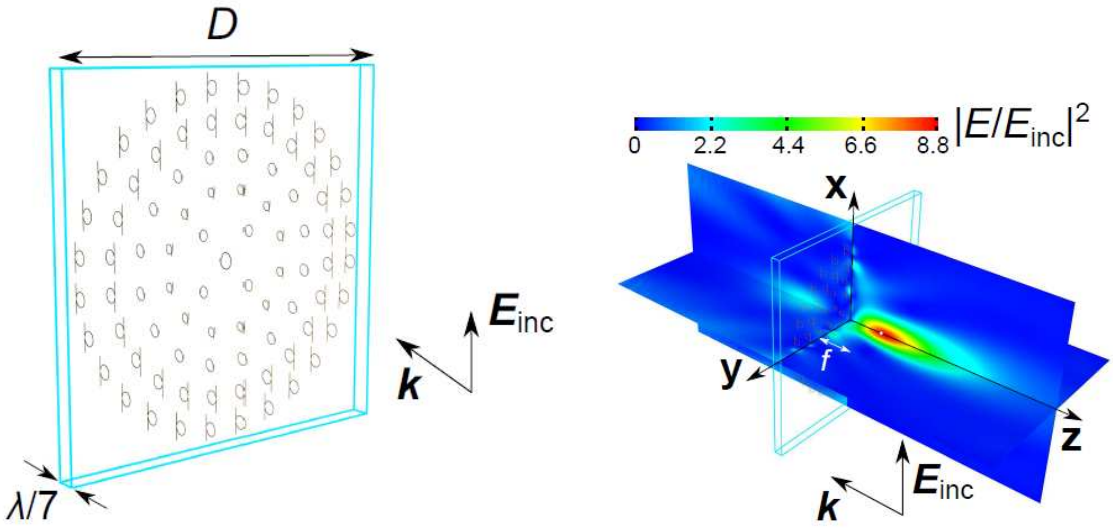

(a) (b)

Figure 6. A focusing metamirror. (a) Model composed of 6 concentric arrays of the designed particles in a dielectric support shown as a box. (b)Reflected and transmitted power density distributions in the $+z$ and $-z$ half-spaces, respectively, normalized to the incident power density.

as they are flat and thin.

The angular stability of the metamirrors is a quite interesting topic which has not been studied before. It could be expected that due to their extremely small focal distances, metamaterial reflectors can face a problem of potentially poor angular stability which can create limitations for the use of such structures. This question is considered in the next section.

3 Angular stability of the focusing metamirror

The question of angular stability has been arisen recently, when the metamirror showed in Figure 6 was represented in conferences. The mirror itself consists of a single-layer periodic array of omega-shaped inclusions located in the unit cell with the area $S = a^2$ (Figure 7).

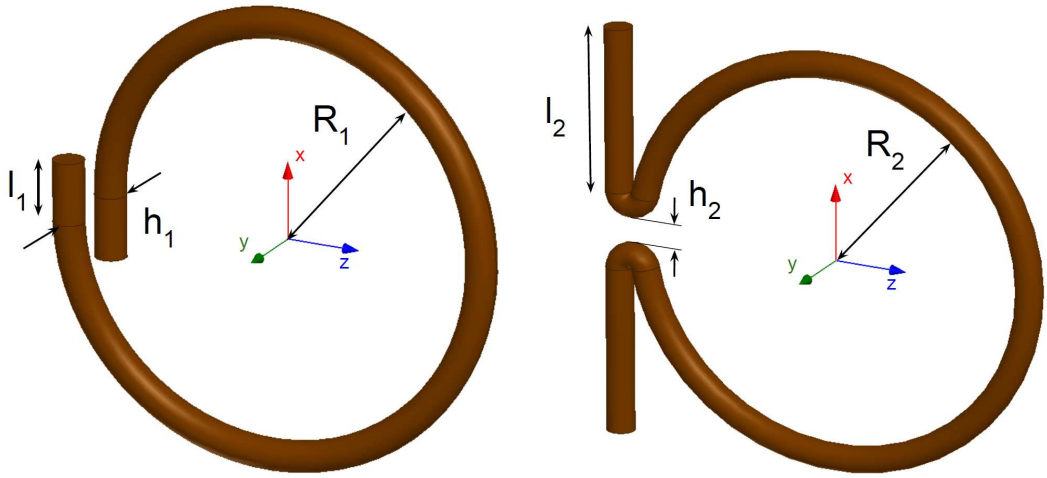

(a) (b)

Figure 7. Two types of omega inclusions. (a) Twisted omega inclusion. (b) Inclusion with the shape of the letter Ω.

Omega particles possess electric and magnetic responses as well as exhibit magnetoelectric coupling, which are characterized by the polarizabilities of the unit cells. The magnetoelectric and electromagnetic polarizabilities describe the ability of the inclusions to obtain electric polarization when they are illuminated by an external magnetic field and magnetic polarization under the effect of an external electric field, respectively. The omega inclusions unite electrically polarizable straight wires which are connected to magnetically polarizable wire loops. In the straight wires an electric dipole moment is excited by an external electric field along the x-axis. Furthermore, a magnetic moment in the loop is excited by the external electric field as well due to the connection between the loop and the straight wires (magnetoelectric coupling). In the same way a magnetic moment in the loop and an electric dipole moment in the straight wire are excited by an external magnetic field along the y-axis. The effect of the magnetoelectric coupling gives more opportunities in designing different metasurfaces, including focusing metamirrors, where it can be used to realize the independent control of reflection and transmission. It should be noted that the loops of the particles are electrically polarizable along the x-axis in addition to the magnetic response. For that reason the electric polarizability of the whole particle amounts to either the difference (Figure 7a) of the polarizabilities of the straight wire and loop, or their sum (Figure 7b). The particles of the first type shown in Figure 7a can effectively reflect electromagnetic waves with the

phases from $-\pi/2$ to $+\pi/2$ and the particles of the second type presented in Figure 7b allow one to cover the range of missing phases from $\pi/2$ to $3\pi/2$. The particles in the metamirror were manually made from copper wire [9, 17].

An incident wave impinges normally on the array surface. The electric and magnetic moments induced in the particles can be considered as surface-averaged electric and magnetic currents so far as the array period is small compared to the wavelength. The currents radiate secondary waves in both forward and backward directions. To achieve zero transmission across the metastructure, the inclusions should conjointly radiate a secondary wave in the forward direction which would interfere with the incident wave destructively: $E_{\rm t} = -E_{\rm inc}$. To provide full reflection with an arbitrary phase ϕ, the backscattered wave must satisfy $E_{\rm ref} = e^{j\phi} E_{\rm inc}$. In the given mirror the phase of reflection from each particle is adjusted individually in order to effectively manage wavefronts of reflection from the structure, maintaining the reflected wave amplitude at the unity value and the necessary phase of the fields scattered in the forward direction. The operating frequency of the present metasurface is 5 GHz.

Use of this metamaterial reflector gives a possibility to replace bulk constructions of reflecting mirrors with a small and thin structure. Therefore, it is important to test the focusing capability during deviations of the incident wave direction from the normal.

3.1 Numerical simulation of the focusing metamirror

As the first step in studying the angular stability of metamirrors we calculated their response numerically. A prototype of the focusing metamirror was modelled in Ansoft HFSS software. The incidence angle deviation varied from 5 to 15 degrees. The power density distributions of the transmitted and the reflected waves normalized to the incident power density were obtained for the different deviation angles of the incident wave (Figure 8). The pictures show that the studied metamirror focuses quite efficiently despite of the incident angle deviation. The numerical data are represented in Table 1.

It is possible to notice that the gain in the focal spot becomes slightly smaller when the incidence becomes oblique. Compared with the other known focusing mirrors and taking into account the extremely short focal distance, the angular stability of the present metamirror can be considered as remarkable. To prove this behaviour of the focusing metastructure, an experimental test has been performed.

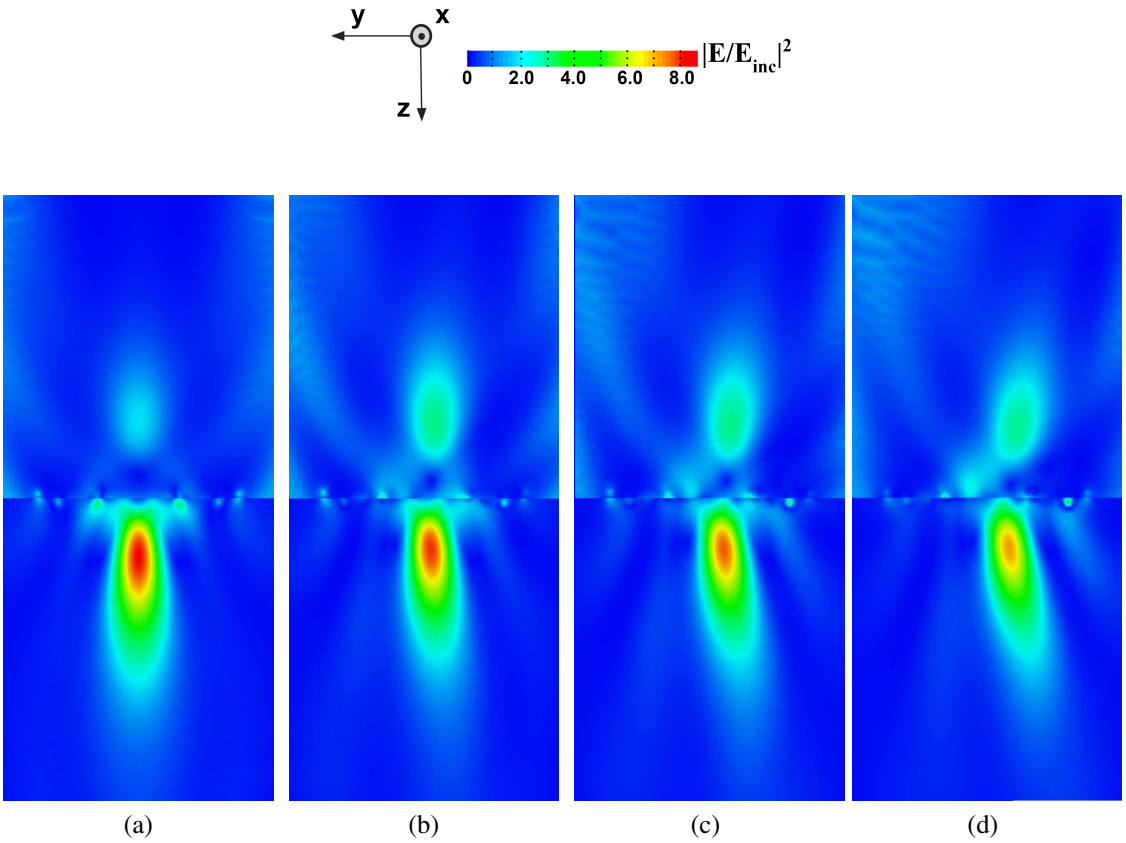

Figure 8. Simulation results. Power density distribution of the transmitted and reflected waves normalized to the incident power density (from right to left): (a) for the normal incidence (gain 8.8); (b) the incident wave is deviated 5 degrees from the normal (gain 8.4); (c) the incident wave is deviated 10 degrees from the normal (gain 8.0); (d) the incident wave is deviated 15 degrees from the normal (gain 7.4).

Table 1. The numerical data of the simulation

Declination of the incident wave from the normal, degrees	Power gain in the shifted focal spot	Deviation of the focal spot, degrees	Power gain in the positions of the initial focal spot
0	8.8	0	8.8
5	8.4	7	7.6
10	8.0	16	5.2
15	7.4	24	2.6
Incident wave (without metamirror)	1	-	-

3.2 Experiment

To verify the stable behaviour of the metamirror, measurements of the field distributions were conducted in a parallel-plate waveguide. Due to the axial symmetry of the metastructure shown in Figure 6a it cannot be analyzed in a planar waveguide. Thus, the metamirror with the symmetry along the xz-plane was manufactured (Figure 9). The parameters of the

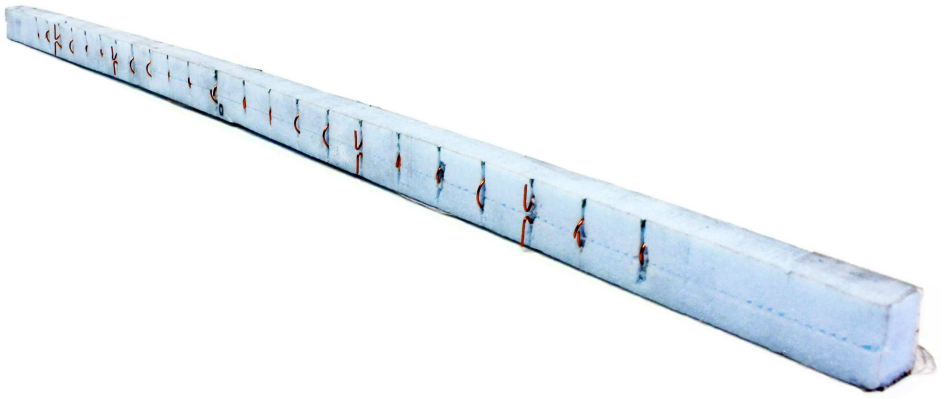

Figure 9. An experimental model of a one-dimensional focusing metamirror consisting of 23 subwavelength manually made copper inclusions which provide a parabolic phase variation of the reflected wavefront.

metamirror inclusions are represented in Appendix 1. This metastructure focuses the reflected waves into a line parallel to the x-axis in the focal plane. Since the particles can be presented as coupled vertical electric and horizontal magnetic dipoles, the two-dimensional scheme of the infinitely periodic structure in the x-direction can be emulated in a parallel-plate waveguide by placing inside a one-dimensional array of the inclusions. The height of the waveguide must be equal to the array period.

A vertical coaxial feed is used as a generator of the incident cylindrical wave with the x-oriented electric field. The analysis of the metamirror is based on the reciprocity principle, which states that the focusing metastructure illuminated by a cylindrical wave from the focal point reflects a plane wave. Hence, the feed is positioned in the the focal spot of the structure. To verify the angular stability, the feed position is changed according to the focal spot positions obtained from the simulations for the different cases of the incident wave deflection. In the waveguide at the operating frequency of the metamirror only transverse electromagnetic (TEM) waves with the fields orthogonal to the direction of propagation can propagate.

In the bottom plate of the waveguide a copper mesh was embedded. Using a movable coaxial probe positioned under the mesh it is possible to measure the spatial distribution of the x-component of the electric field inside the waveguide. The mesh period is much smaller

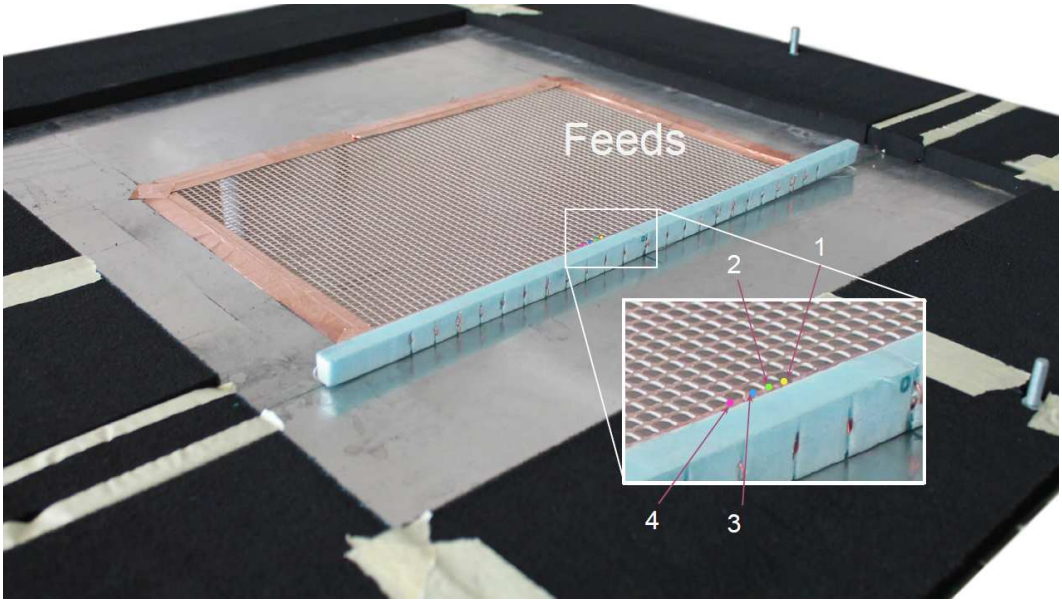

Figure 10. Experimental setup. The bottom part of the waveguide with the mesh and metamirror. Feeds are marked by numbers: 1 – location of the feed for the normally reflected plane wave, 2 – location of the feed for the simulated reflected plane wave at 5 degrees angle (5 mm displacement from 1), 3 – location of the feed for the simulated reflected plane wave at 10 degrees angle (11 mm displacement from 1), 4 – location of the feed for the simulated reflected plane wave at 15 degrees angle (17.5 mm displacement from 1).

than the wavelength, therefore the field distribution inside is not significantly disturbed by the mesh. Two sets of measurements are needed to determine the distribution of the reflected fields from the metamirror. First, we measure the field distribution in an empty waveguide to obtain the field distribution of the incident wave. The second set of measurements gives the total electric field in the waveguide with the metamirror placed inside. By knowing the field distribution of the incident wave and the total field it is possible to find the reflected field distribution by subtracting one from the other.

The experimental setup is shown in Figure 11. The parallel-plate waveguide has the following dimensions: the height along the x-axis is 15 mm, the width equals 80 cm along the y-axis and 90 cm along the z-axis. The vertical coaxial feed is located at the focal distance of $F = 0.65\lambda = 39$ mm from the metamirror on the z-axis. The feed coordinates along the y-axis are changed from the focal spot of the normal incidence case. For the cases of 7, 16, 24 degrees deflection of the focal spot from the normal the distances are 5 mm, 11 mm and 17.5 mm, respectively. The position of the manufactured one-dimensional metamirror is parallel to the edge of the waveguide at the distance F from the beginning of the mesh. The size of the mesh is 25 cm by 35 cm and the period is 5 mm with the strip width of 1 mm. The center of the mesh is positioned at the distance of 161 mm from the metamirror. A vertical coaxial probe located 5 mm below the mesh gauges the near fields penetrated through the

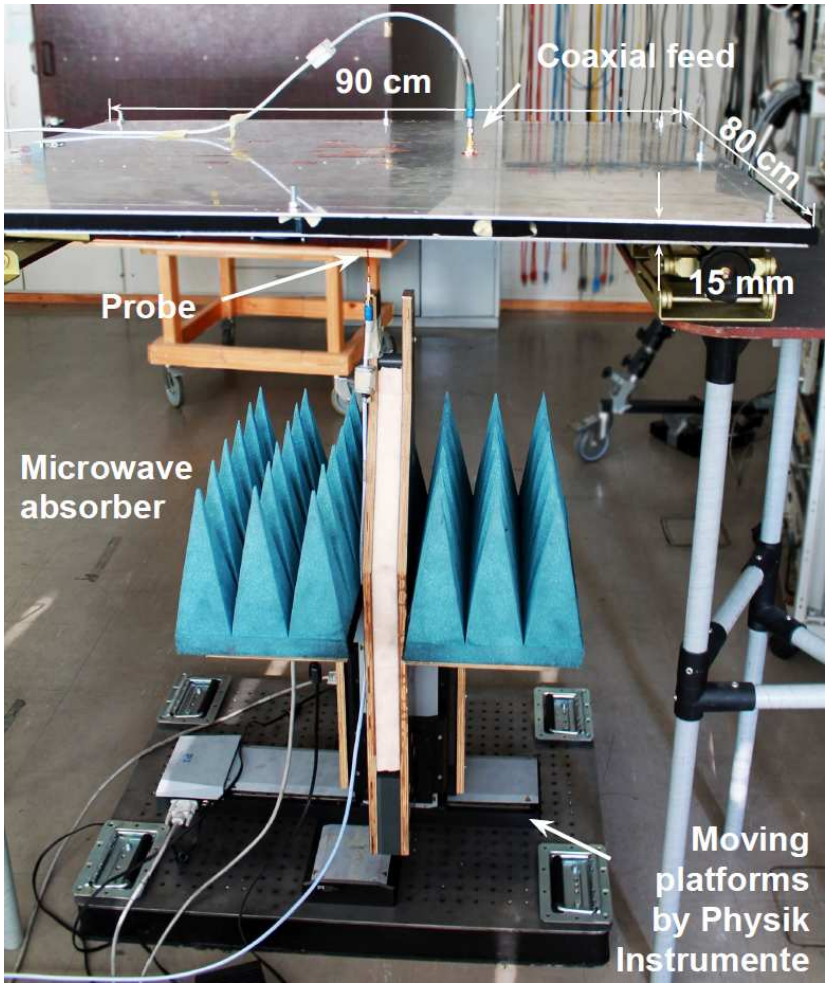

Figure 11. Experimental construction: the moving platforms (Physik Instrumente), coaxial probe antenna, coaxial feed antenna and parallel-plate waveguide.

mesh. To reduce parasitic reflections from the edges of the waveguide, it was necessary to place microwave absorbing material blocks of 10 cm width at the edges of the waveguide. The measuring device in the experiment is a vector network analyzer Agilent Technologies E8363A. Port 1 and port 2 of the analyzer should be connected to the stationary coaxial feed and to the movable coaxial probe, respectively. To scan the fields under the mesh in the horizontal plane, two moving platforms (manufactured by Physik Instrumente) along the $y-$ and z-directions are in use. The vector analyzer and a PC were connected to these platforms. The transmission coefficient S_{21} from port 1 to port 2 is measured by the scanning system with the step of 10 mm. The distribution of the x-component of the electric field is represented by the spatial distribution of the transmission coefficient.

The results obtained in the experiment are represented in Figure 12 – 14. The field distribution of the incident wave in the empty waveguide for the 5 mm, 11 mm and 17.5 mm feed displacement are shown in Figure 12a, Figure 13a and Figure 14a, respectively. Figure 12b,

Figure 13b and Figure 14b show corresponding total field distributions in the waveguide with the presence of the metamirror.

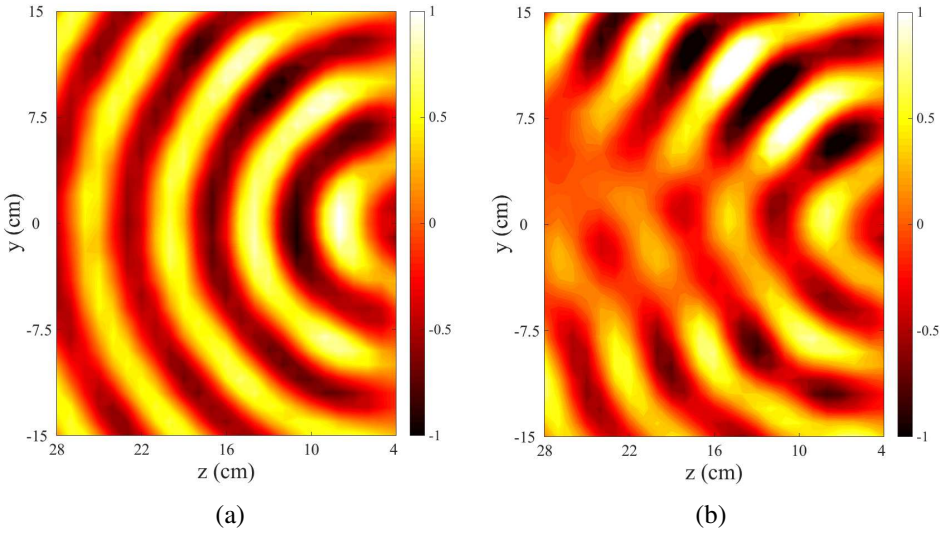

Figure 12. Experimental data for the 7 degrees inclination of the coaxial feed from the normal. (a) The field distribution of the incident cylindrical wave radiated in the empty waveguide. (b) The total field distribution of the incident and reflected waves with the presence of the focusing metamirror.

Data for the field distribution of the reflected wave from the metasurface for all three cases of different feed displacement are presented in Figure 15. It is possible to see the plane waves deflected at some angles. The 11, 20 and 23 degrees deflections are represented in

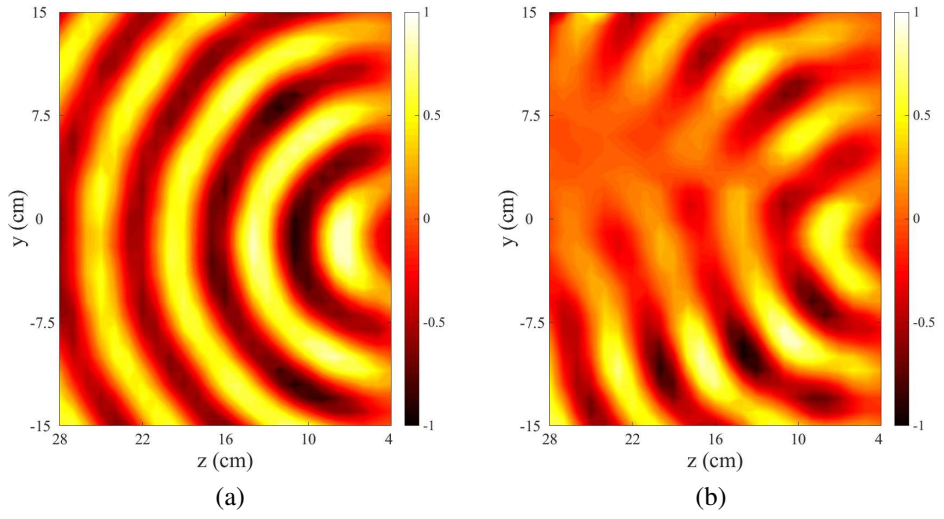

Figure 13. Experimental data for the 16 degrees inclination of the coaxial feed from the normal. (a) The field distribution of the incident cylindrical wave radiated in the empty waveguide. (b) The total field distribution of the incident and reflected waves with the presence of the focusing metamirror.

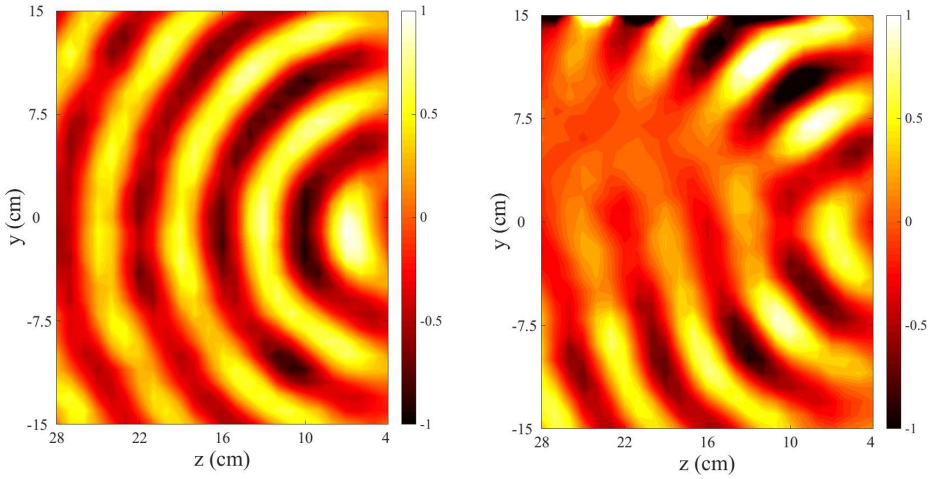

Figure 14. Experimental data for the 24 degrees inclination of the coaxial feed from the normal. (a) The field distribution of the incident cylindrical wave radiated in the empty waveguide. (b) The total field distribution of the incident and reflected waves with the presence of the focusing metamirror.

Figure 15a, Figure 15b and Figure 15c, respectively. The metamirror has a finite (and rather small) length, therefore, the bottom part of the pictures is blurred.

In conclusion, the simulation and experiment verifying the angular stability of the focusing metamirror show the unique benefits of its usage. Relatively stable to changes of the angle of incidence, compact, penetrable in the non-operational frequency range, easily tunable focusing metastructure can be employed in many different applications.

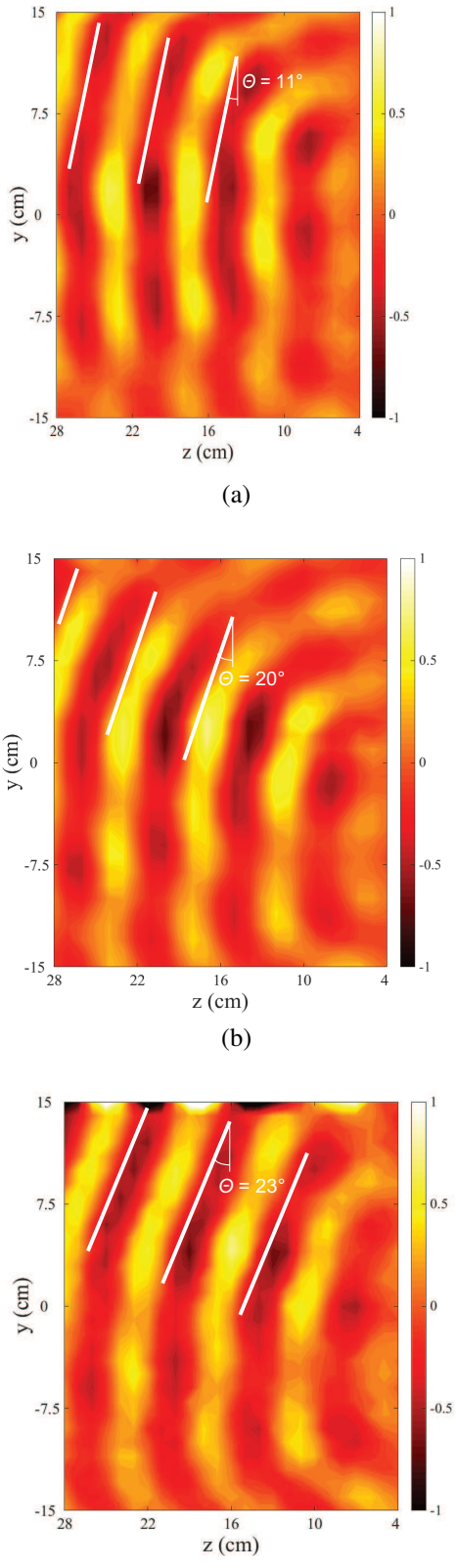

Figure 15. Experimental results. The field distribution of the wave reflected from the metamirror. For the displacements of the feed equal to 5 mm, 11 mm and 17.5 mm the inclinations of the plane wave from the normal are (a) 11 degrees, (b) 20 degrees, (c) 23 degrees, respectively.

4 New concept of metamirrors

The known methods of metamirror designs, including that introduced in [17] and studied in the above sections, are not ideal. The design in [17] is based on the physical-optics approximation, and it is assured that at every point of the aperture the incident plane wave produces a reflected plane wave with the required phase. To tune the shapes and dimensions of the array particles, the formulas for reflection and transmission coefficients for a uniform array illuminated by a normally incident plane wave are used. Thus, although the reflection phase at each point is tuned to be correct, the wave impedance of the reflected wave is not equal to what is ideally desired (namely, the reflected wave propagates in a direction which is different than the normal direction). Here we attack the problem of finding the shapes and dimensions of inclusions such that the reflected and transmitted fields would satisfy the required boundary conditions *exactly*.

To design a metasurface that deflects the incident waves at an arbitrary chosen angle, three strict requirements should be fulfilled. First of them is to ensure a zero value of the amplitude of the transmitted wave. The second requirement says that a correct phase variation over the surface of the metamirror should be created. And the last one requires the correct orientation of the wave vector k, electric E and magnetic H field vectors of the reflected plane wave.

All the known metamirror structures [18–25] are designed using the concept shown in Figure 16a. The surface with a linearly changing phase of the reflection coefficient reflects a normally incident wave at a chosen angle with a nearly plane wavefront which is created by many spherical wavefronts produced by each inclusion. It should be stressed that the last requirement of the correct vectors orientation is not fulfilled in this case and the locally-reflected wave does not change its direction. Thus, such a way is approximate and not perfect, which is a significant drawback of this concept.

In this thesis a different concept of metasurface operation is introduced. The main idea of it is to synthesise appropriate surface currents in the structure which satisfy all the three requirements (Figure 16b). The synthesis is based on Huygens' principle [26–28].

To understand the whole concept, it is necessary to introduce a theoretical basis, such as the Maxwell equations, boundary conditions and Huygens' principle.

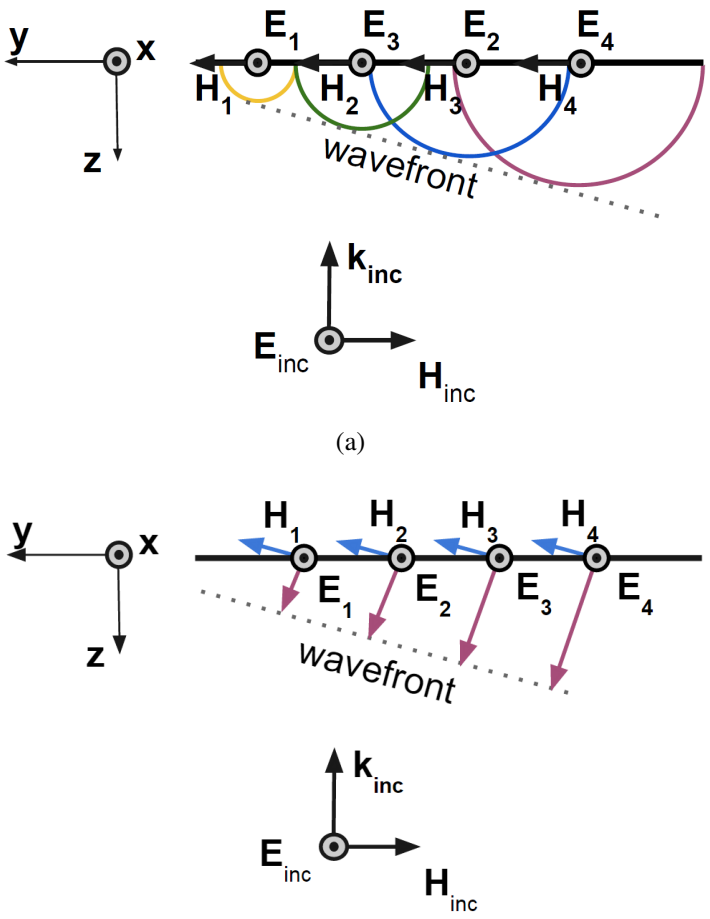

Figure 16. Different concepts of metamirror operation. (a) Previously considered idea representing a plane wavefront created by multiple spherical wavefronts. (b) The idea based on Huygens' principle comprising the plane wavefront created through the declination of the wave propagation direction.

4.1 Maxwell's equations

The Maxwell equations are a set of fundamental equations describing behaviour of electric and magnetic fields. James Clerk Maxwell was the person who has written them down in a complete form. The equations are highly symmetric and they can be cast in many forms using different mathematical formalisms. The Maxwell equations (in the present work it is a modified set of Maxwell's equations) are written in terms of the electric and magnetic field vectors E, H and the electric and magnetic flux densities D, B:

$$\nabla \cdot D = \rho_{\mathrm{e}}, \tag{4}$$

$$\nabla \cdot B = \rho_{\mathrm{m}}, \tag{5}$$

$$\nabla \times E = -J_{\mathrm{m}} - \frac{\partial B}{\partial t}, \tag{6}$$

$$\nabla \times H = J_{\mathrm{e}} + \frac{\partial D}{\partial t}. \tag{7}$$

Here, the electric J_{e} and magnetic J_{m} current densities, the electric ρ_{e} and the magnetic ρ_{m} charge densities describe sources of electromagnetic fields (for example, [29]).

4.2 Boundary Conditions

An interface between two different media is modelled by boundary conditions for the electromagnetic field vectors which can be derived from the integral form of the Maxwell equations. The boundary conditions for the tangential components of the electric and magnetic fields are written as

$$\begin{aligned} n \times (H_1 - H_2) &= J_{\mathrm{se}}, \\ n \times (E_1 - E_2) &= -J_{\mathrm{sm}}, \end{aligned} \tag{8}$$

where J_{se} and J_{sm} are electric and magnetic surface current densities, accordingly. The boundary conditions for the normal components of the fields:

$$\begin{aligned} n \cdot (D_1 - D_2) &= \rho_{\mathrm{se}}, \\ n \cdot (B_1 - B_2) &= \rho_{\mathrm{sm}}, \end{aligned} \tag{9}$$

where ρ_{se} and ρ_{sm} are electric and magnetic surface charge densities, respectively.

Any set of fields which at once satisfy Maxwell equations and boundary conditions for the tangential components of the field will automatically satisfy the conditions for the normal components. When an incident wave traverses the interface, reflected and refracted waves with different amplitudes occur, and these amplitudes can be found knowing the boundary conditions.

4.3 Huygens' principle

Huygens' principle was formulated by a Dutch scientist Christiaan Huygens in the seventeenth century. He was inspired by the Robert Hooke's first proposal about a wave theory of light. The principle tells that actual volumetric sources can be replaced by equivalent sources on a closed surface enclosing the actual sources [30]. Later, in 1936, a more mathematical formulation of Huygens' principle, known as the field equivalence principle, was introduced

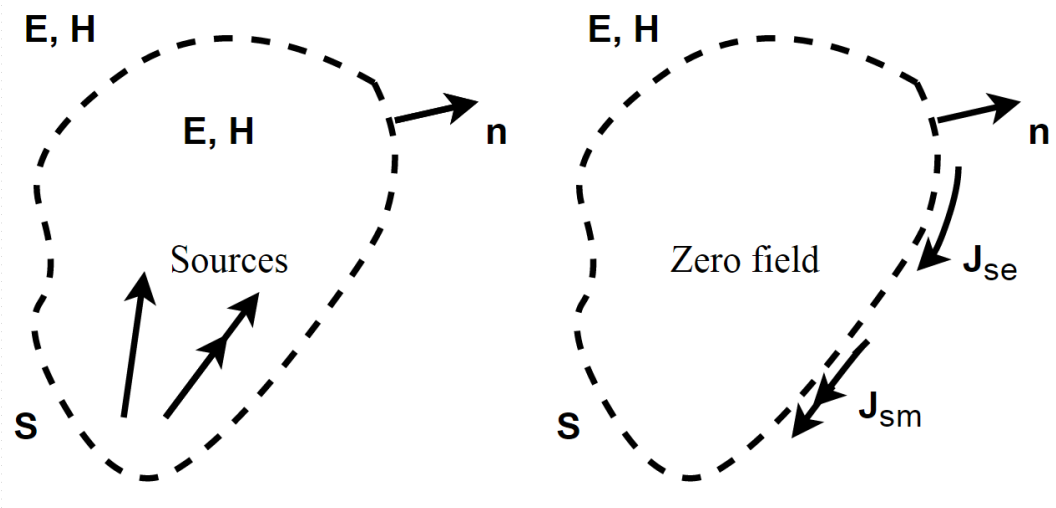

Figure 17. Huygens' principle. Actual and equivalent problem models.

by prof. Sergei Schelkunoff. It states that an arbitrary volume with sources can be represented as a closed surface with the appropriate electric and magnetic current densities which meet the boundary conditions (Figure 17). The selected current densities should provide zero fields inside the closed surface and fields equal to the radiation created by the actual sources outside of the volume [31].

4.4 A new point of view

Let us consider the incidence of an infinite plane wave on a metasurface which reflects the wave at an angle as it is shown in Figure 16b. This issue can be brought to the boundary problem at the interface between two media (in the present work two half-spaces separated by a sheet of electric and magnetic currents). In this section the surface current densities which are required to provide the mode shown in Figure 16b are determined.

An incident plane wave impinges normally on the interface (Figure 18). The field vectors of the incident wave are described by the equations:

$$\begin{aligned} E_{\text{inc}} &= x\, E_{\text{inc}}, \\ H_{\text{inc}} &= -y\, H_{\text{inc}} = -y\, \frac{E_{\text{inc}}}{\eta_0}, \end{aligned} \tag{10}$$

where η_0 is the wave impedance of free space.

Using Huygens' principle, one should require zero fields behind the interface (the $-z$ half-space) and the tilted reflected wave in front of the interface (the $+z$ half-space). It is im-

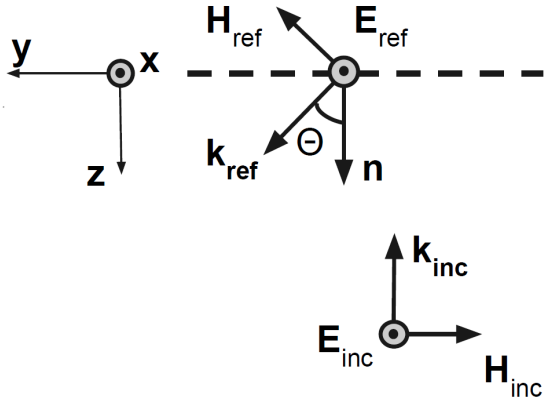

Figure 18. Huygens' principle for the metasurface. The normally incident wave reflected at an angle θ from the normal with zero transmission.

portant to notice that the amplitude of the reflected wave will be different from the incident wave. Ariel Epstein and George Eleftheriades in their article [27] considered a Huygens' metasurface which declines transmitted waves by a specific angle. In that work the transmitted wave amplitude was equal to the amplitude of the incident wave. They stressed that for the case of transmittarrays the existence of reflection is a required condition, otherwise the local power conservation law is not valid. As it was mentioned above, the task of a reflectarray is similar to the transmittarray, therefore the statement would mean some unavoidable non-zero transmission in the reflecting metamirror. The obstacle mentioned in [27] can be overcome considering the areas of reflected and incident beams. Figure 19 shows that after reflection from the metasurface the beam of the wave becomes narrower.

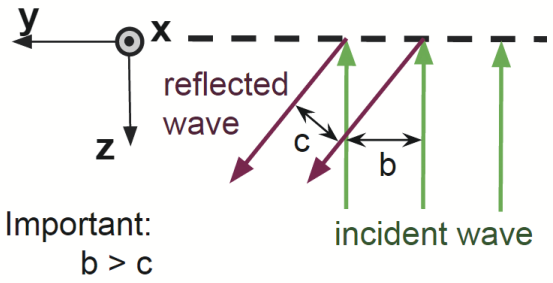

Figure 19. An important note: the incident beam is wider than the reflected beam.

Therefore, in order to satisfy the energy conservation in a zero-transmittance metamirror, the power of the wave reflected from the metasurface should be $1/\cos\theta$ times higher then that

of the incident wave. Thus, the reflected electric field is expressed as follows:

$$E_{\mathrm{ref}} = \frac{E_{\mathrm{inc}}}{\sqrt{\cos\theta}}\, e^{j\phi} = x\, \frac{E_{\mathrm{inc}}}{\sqrt{\cos\theta}}\, e^{j\phi}, \tag{11}$$

where θ is the desired angle of inclination and ϕ is the relative phase of the reflected wave which is a function of the y-coordinate.
The wave vector k can be found using the projections on the x- and y-axes:

$$k_{\mathrm{ref}} = y \sin\theta + z \cos\theta. \tag{12}$$

To find the magnetic field vector, the relation between E, H and k is used:

$$k_{\mathrm{ref}} \times E_{\mathrm{ref}} = \eta_0 H_{\mathrm{ref}}. \tag{13}$$

Combining (11), (12) and (13):

$$H_{\mathrm{ref}} = \frac{1}{\eta_0}(y \sin\theta + z \cos\theta) x\, \frac{E_{\mathrm{inc}}}{\sqrt{\cos\theta}}\, e^{j\phi} = (y \cos\theta - z \sin\theta) \frac{E_{\mathrm{inc}}}{\eta_0 \sqrt{\cos\theta}}\, e^{j\phi}. \tag{14}$$

The next step is to find the required electric and magnetic surface current densities. Since the reflected wave satisfies the Maxwell equations (being a solution in the form of (13)), it is enough to use the boundary conditions only for the tangential components of the fields (8):

$$\begin{aligned} J_{\mathrm{se}} &= n \times (H_{\mathrm{inc}} + H_{\mathrm{ref}}), \\ J_{\mathrm{sm}} &= -n \times (E_{\mathrm{inc}} + E_{\mathrm{ref}}). \end{aligned} \tag{15}$$

Applying equations (11) and (14), the surface current densities are written as follows:

$$\begin{aligned} J_{\mathrm{se}} &= \frac{E_{\mathrm{inc}}}{\eta_0}\, (1 - \sqrt{\cos\theta}\, e^{j\phi}), \\ J_{\mathrm{sm}} &= H_{\mathrm{inc}}\, \eta_0\, (1 + \frac{e^{j\phi}}{\sqrt{\cos\theta}}). \end{aligned} \tag{16}$$

Equations (16) show the surface current densities at the interface which create the necessary field distributions in both the $+z$ and $-z$ half-spaces. The electric J_{se} and magnetic J_{sm} current densities can be modelled as a discrete planar array of electric p and magnetic m dipole moments which can also be determined by the effective electric $\overline{\overline{\hat{\alpha}}}_{\mathrm{ee}}$, magnetic $\overline{\overline{\hat{\alpha}}}_{\mathrm{mm}}$, electro-

magnetic $\overline{\overline{\hat{\alpha}}}_{\mathrm{em}}$ and magneto-electric $\overline{\overline{\hat{\alpha}}}_{\mathrm{me}}$ polarizability dyadics of the constituent inclusions:

$$\begin{aligned} \boldsymbol{J}_{\mathrm{se}} &= \frac{j\omega \boldsymbol{p}}{S} = j\,\frac{\omega}{S}\,(\overline{\overline{\hat{\alpha}}}_{\mathrm{ee}} \cdot \boldsymbol{E}_{\mathrm{inc}} + \overline{\overline{\hat{\alpha}}}_{\mathrm{em}} \cdot \boldsymbol{H}_{\mathrm{inc}}), \\ \boldsymbol{J}_{\mathrm{sm}} &= \frac{j\omega \boldsymbol{m}}{S} = j\,\frac{\omega}{S}\,(\overline{\overline{\hat{\alpha}}}_{\mathrm{mm}} \cdot \boldsymbol{H}_{\mathrm{inc}} + \overline{\overline{\hat{\alpha}}}_{\mathrm{me}} \cdot \boldsymbol{E}_{\mathrm{inc}}), \end{aligned} \tag{17}$$

where $S = a^2$ is the area of the unit cell of the array.

It is convenient to describe the metasurface in terms of the polarizabilities of its inclusions. Combining (16) and (17), it is possible to derive the following conditions to determine the required effective polarizabilities:

$$\begin{aligned} 1 - \sqrt{cos\theta}\, e^{j\phi} &= j\,\frac{\omega}{S}\,(\hat{\alpha}_{\mathrm{ee}}^{\mathrm{xx}}\,\eta_0 - \hat{\alpha}_{\mathrm{em}}^{\mathrm{xy}}), \\ 1 + \frac{e^{j\phi}}{\sqrt{cos\theta}} &= j\,\frac{\omega}{S}\,(\frac{\hat{\alpha}_{\mathrm{mm}}^{\mathrm{yy}}}{\eta_0} - \hat{\alpha}_{\mathrm{me}}^{\mathrm{yx}}). \end{aligned} \tag{18}$$

Based on the results in [13], in the present work omega-shaped inclusions of the metastructure are in consideration. To resolve the system of equations (18), the relation between the effective polarizabilities for omega particles made of a single piece of metal wire or strip [13] can be applied:

$$\hat{\alpha}_{\mathrm{ee}}^{\mathrm{xx}}\,\hat{\alpha}_{\mathrm{mm}}^{\mathrm{yy}} = -(\hat{\alpha}_{\mathrm{em}}^{\mathrm{xy}})^2. \tag{19}$$

Therefore,

$$\begin{aligned} \hat{\alpha}_{\mathrm{em}}^{\mathrm{xy}} &= \sqrt{-\hat{\alpha}_{\mathrm{ee}}^{\mathrm{xx}}\,\hat{\alpha}_{\mathrm{mm}}^{\mathrm{yy}}}, \\ \hat{\alpha}_{\mathrm{me}}^{\mathrm{yx}} &= -\sqrt{-\hat{\alpha}_{\mathrm{ee}}^{\mathrm{xx}}\,\hat{\alpha}_{\mathrm{mm}}^{\mathrm{yy}}}. \end{aligned} \tag{20}$$

Now using formulas (18) and (20), the solution for the system can be obtained:

$$\hat{\alpha}_{\mathrm{ee}}^{\mathrm{xx}} = j\,\frac{S\,\sqrt{\cos\theta}\,(1 - \sqrt{\cos\theta}\,e^{j\phi})^2}{\omega\,\eta_0\;e^{j\phi}(1+\cos\theta)}, \tag{21}$$

$$\hat{\alpha}_{\mathrm{mm}}^{\mathrm{yy}} = -j\,\frac{\eta_0\,S\,(\sqrt{\cos\theta} + e^{j\phi})^2}{\omega\,\sqrt{\cos\theta}\,e^{j\phi}(1+\cos\theta)}, \tag{22}$$

$$\hat{\alpha}_{\mathrm{em}}^{\mathrm{xy}} = j\,\frac{S\,(\sqrt{\cos\theta} + e^{j\phi})(1 - \sqrt{\cos\theta}\,e^{j\phi})}{\omega\,e^{j\phi}(1+\cos\theta)}, \tag{23}$$

$$\hat{\alpha}_{\mathrm{me}}^{\mathrm{yx}} = -j\,\frac{S\,(\sqrt{\cos\theta}+e^{j\phi})(1-\sqrt{\cos\theta}\,e^{j\phi})}{\omega\,e^{j\phi}(1+\cos\theta)}. \tag{24}$$

From these equations it is possible to obtain the individual polarizability values of each inclusion [13]:

$$\alpha_{\mathrm{ee}}^{\mathrm{xx}} = \frac{\hat{\alpha}_{\mathrm{ee}}^{\mathrm{xx}} + \beta_{\mathrm{m}}\,(\hat{\alpha}_{\mathrm{ee}}^{\mathrm{xx}}\hat{\alpha}_{\mathrm{mm}}^{\mathrm{yy}} + \hat{\alpha}_{\mathrm{em}}^{\mathrm{xy}}\hat{\alpha}_{\mathrm{me}}^{\mathrm{yx}})}{1+(\hat{\alpha}_{\mathrm{ee}}^{\mathrm{xx}}\beta_{\mathrm{e}} + \hat{\alpha}_{\mathrm{mm}}^{\mathrm{yy}}\beta_{\mathrm{m}}) + \beta_{\mathrm{e}}\beta_{\mathrm{m}}\,(\hat{\alpha}_{\mathrm{ee}}^{\mathrm{xx}}\hat{\alpha}_{\mathrm{mm}}^{\mathrm{yy}} + \hat{\alpha}_{\mathrm{em}}^{\mathrm{xy}}\hat{\alpha}_{\mathrm{me}}^{\mathrm{yx}})}, \tag{25}$$

$$\alpha_{\mathrm{mm}}^{\mathrm{yy}} = \frac{\hat{\alpha}_{\mathrm{mm}}^{\mathrm{yy}} + \beta_{\mathrm{e}}\,(\hat{\alpha}_{\mathrm{ee}}^{\mathrm{xx}}\hat{\alpha}_{\mathrm{mm}}^{\mathrm{yy}} + \hat{\alpha}_{\mathrm{em}}^{\mathrm{xy}}\hat{\alpha}_{\mathrm{me}}^{\mathrm{yx}})}{1+(\hat{\alpha}_{\mathrm{ee}}^{\mathrm{xx}}\beta_{\mathrm{e}} + \hat{\alpha}_{\mathrm{mm}}^{\mathrm{yy}}\beta_{\mathrm{m}}) + \beta_{\mathrm{e}}\beta_{\mathrm{m}}\,(\hat{\alpha}_{\mathrm{ee}}^{\mathrm{xx}}\hat{\alpha}_{\mathrm{mm}}^{\mathrm{yy}} + \hat{\alpha}_{\mathrm{em}}^{\mathrm{xy}}\hat{\alpha}_{\mathrm{me}}^{\mathrm{yx}})}, \tag{26}$$

$$\alpha_{\mathrm{em}}^{\mathrm{xy}} = \frac{\hat{\alpha}_{\mathrm{em}}^{\mathrm{xy}}}{1+(\hat{\alpha}_{\mathrm{ee}}^{\mathrm{xx}}\beta_{\mathrm{e}} + \hat{\alpha}_{\mathrm{mm}}^{\mathrm{yy}}\beta_{\mathrm{m}}) + \beta_{\mathrm{e}}\beta_{\mathrm{m}}\,(\hat{\alpha}_{\mathrm{ee}}^{\mathrm{xx}}\hat{\alpha}_{\mathrm{mm}}^{\mathrm{yy}} + \hat{\alpha}_{\mathrm{em}}^{\mathrm{xy}}\hat{\alpha}_{\mathrm{me}}^{\mathrm{yx}})}, \tag{27}$$

$$\alpha_{\mathrm{me}}^{\mathrm{yx}} = \frac{\hat{\alpha}_{\mathrm{me}}^{\mathrm{yx}}}{1+(\hat{\alpha}_{\mathrm{ee}}^{\mathrm{xx}}\beta_{\mathrm{e}} + \hat{\alpha}_{\mathrm{mm}}^{\mathrm{yy}}\beta_{\mathrm{m}}) + \beta_{\mathrm{e}}\beta_{\mathrm{m}}\,(\hat{\alpha}_{\mathrm{ee}}^{\mathrm{xx}}\hat{\alpha}_{\mathrm{mm}}^{\mathrm{yy}} + \hat{\alpha}_{\mathrm{em}}^{\mathrm{xy}}\hat{\alpha}_{\mathrm{me}}^{\mathrm{yx}})}, \tag{28}$$

where β_{e} and β_{m} are the electric- and magnetic-field interaction constants. They can be approximately (the imaginary parts, responsible for the energy conservation, are exact) found as follows [32]:

$$\begin{aligned}
\beta_{\mathrm{e}} &= \mathrm{Re}\left(-\frac{jk_0}{4\varepsilon_0\,S}\left[1-\frac{1}{jk_0\rho}\right]e^{-jk_0\rho}\right) + j\,\frac{k_0^3}{6\pi\varepsilon} - j\,\frac{\eta_0\,\omega}{2S},\\
\beta_{\mathrm{m}} &= \mathrm{Re}\left(-\frac{jk_0}{4\varepsilon_0\eta_0^2\,S}\left[1-\frac{1}{jk_0\rho}\right]e^{-jk_0\rho}\right) + j\,\frac{k_0^3}{6\pi\varepsilon\eta_0^2} - j\,\frac{\eta_0\,\omega}{2S\eta_0}\,\cos\theta,
\end{aligned} \tag{29}$$

where $\rho = a/1.438$, k_0 is the wavenumber of free space, and ω is the angular frequency.

Using (21)-(29), numerical calculations with MatLAB software were carried out. Analyzing the results on the level of the polarizabilities, the power conservation law was, however, not exactly satisfied. The reason for this can be in not complete understanding and deficiency of the developed theory, or else it may be so that it is impossible to realize an ideally lossless wavefront shaping metasurface which has exactly zero transmittance. In fact, a similar statement is made in [27] for transmittarrays, but in that paper the theory is based on some approximations, practically equivalent to the physical optics approximation. Clearly, this important issue needs further study.

4.5 Energy conservation

To prove the energy conservation in the system, we evaluate the power balance in terms of electric and magnetic dipole moments induced in the unit cells. The structure of the particles in the studied metamirror can be described through two sets of dipole moments: one is responsible for the tilted reflection and another one for the incident wave cancellation behind the mirror.

The electric dipole moment is in consideration. For the reflection with the phase changing over the structure area we require that

$$p = p_1\, e^{-jk_0 \sin\theta y} + p_2 = \alpha_{\rm ee}(y)\,(E_{\rm inc} + \beta_{\rm e1}\, p_1\, e^{-jk_0 \sin\theta y} + \beta_{\rm e2}\, p_2), \tag{30}$$

where $\beta_{\rm e1}$ and $\beta_{\rm e2}$ are the electric-field interaction constants for the dipole moment arrays p_1 and p_2, respectively. The dipole moment is related to the surface current and it can be derived from (17):

$$\begin{aligned} p_1 &= \frac{S\,E_{\rm inc}}{j\omega\eta_0}\,\sqrt{\cos\theta}\,e^{j\phi_0}, \\ p_2 &= -\frac{S\,E_{\rm inc}}{j\omega\eta_0}, \end{aligned} \tag{31}$$

where ϕ_0 is the reflection phase at $y = 0$.

Since the imaginary part is more important for this goal, it is possible to write the electric-field interaction constants as:

$$\begin{aligned} \beta_{\rm e1} &= {\rm Re}(\beta) + j\,\frac{k^3}{6\pi\varepsilon} - j\,\frac{\eta_0\,\omega}{2S\,\cos\theta}, \\ \beta_{\rm e2} &= {\rm Re}(\beta) + j\,\frac{k^3}{6\pi\varepsilon} - j\,\frac{\eta_0\,\omega}{2S}. \end{aligned} \tag{32}$$

Combining (30), (31) and(32), absorption in the particles can be analysed:

$${\rm Im}\left(\frac{1}{\alpha_{\rm ee}}\right) = \frac{k^3}{6\pi\varepsilon} - \frac{\dfrac{\eta_0\,\omega}{2S}\,\sqrt{\cos\theta}\,\cos(\phi_0 - k_0\sin\theta y)\,\left(1 - \dfrac{1}{\cos\theta}\right)}{1 - 2\sqrt{\cos\theta}\,\cos(\phi_0 - k_0\sin\theta y) + \cos\theta}. \tag{33}$$

In the same way one can get equations for the magnetic dipole moment and the magnetic-

field interaction constants:

$$\boldsymbol{m} = \boldsymbol{m}_1\, e^{-jk_0 \sin\theta y} + \boldsymbol{m}_2 = \alpha_{\mathrm{mm}}(y)\,(\boldsymbol{H}_{\mathrm{inc}} + \beta_{\mathrm{m1}}\,\boldsymbol{m}_1\, e^{-jk_0 \sin\theta y} + \beta_{\mathrm{m2}}\,\boldsymbol{m}_2), \tag{34a}$$

$$\boldsymbol{m}_1 = \frac{S\eta_0\,\boldsymbol{H}_{\mathrm{inc}}}{j\omega}\,\frac{e^{j\phi_0}}{\sqrt{\cos\theta}}, \tag{34b}$$

$$\boldsymbol{m}_2 = \frac{S\eta_0\,\boldsymbol{H}_{\mathrm{inc}}}{j\omega}, \tag{34c}$$

$$\beta_{\mathrm{m1}} = \frac{\mathrm{Re}(\beta)}{\eta_0^2} + j\,\frac{k^3}{6\pi\varepsilon\eta_0^2} - j\,\frac{\eta_0\,\omega}{2S\eta_0}\,\cos\theta, \tag{34d}$$

$$\beta_{\mathrm{m2}} = \frac{\mathrm{Re}(\beta)}{\eta_0^2} + j\,\frac{k^3}{6\pi\varepsilon\eta_0^2} - j\,\frac{\eta_0\,\omega}{2S\eta_0}. \tag{34e}$$

The imaginary part of the individual-particle magnetic polarizability takes the form:

$$\mathrm{Im}\left(\frac{1}{\alpha_{\mathrm{mm}}}\right) = \frac{k^3}{6\pi\varepsilon\eta_0^2} + \frac{\dfrac{\omega\,\cos(\phi_0 - k_0\sin\theta y)}{2S\eta_0\,\sqrt{\cos\theta}}\,(1-\cos\theta)}{1 + 2\,\dfrac{\cos(\phi_0 - k_0\sin\theta y)}{\sqrt{\cos\theta}} + \frac{1}{cos\theta}}. \tag{35}$$

When $\theta = 0$, the expressions for effective electric and magnetic polarizabilities may be simplified:

$$\begin{aligned} \mathrm{Im}\left(\frac{1}{\alpha_{\mathrm{ee}}}\right) &= \frac{k^3}{6\pi\varepsilon}, \\ \mathrm{Im}\left(\frac{1}{\alpha_{\mathrm{mm}}}\right) &= \frac{k^3}{6\pi\varepsilon\eta_0^2}. \end{aligned} \tag{36}$$

These equations show that there is no absorption in the particles, but in the case of oblique reflection it is not valid. Therefore, it is necessary to analyze the hypothesis from the beginning.

4.6 Verification of the assumption

To verify the validity of the considered assumptions, it is necessary to check the equations for the surface current densities. The electric current (16) creates the scattered fields in front of the structure (area 1) and behind the structure (area 2). It is represented in Figure 20. As it was stated before, there are two components in the expression for the surface current density: one of them is responsible for the creation of the normally-propagating plane wave field distribution and another one for the creation of the tilted field distribution. Thus, the picture shows that in area 2 there are two scattered waves: one propagates in the direction opposite to the normal and another one is declined from the normal at an angle $\pi - \theta$. In the

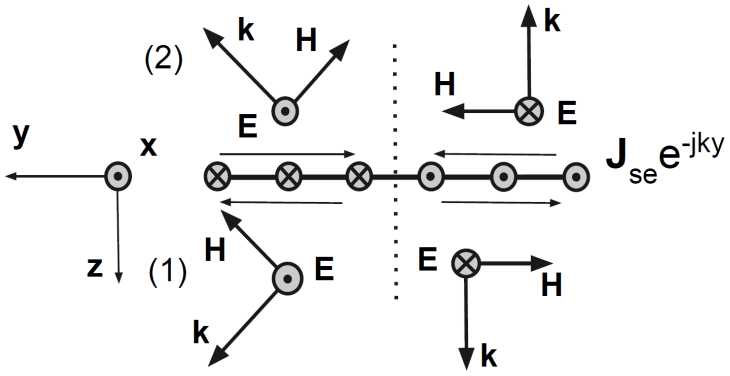

Figure 20. Scattered fields created by the electric surface current in both $-z$ (area 2) and $+z$ (area 1) half-spaces. Dots line is pictured to distinguish the two components of the electric surface current density with different signs.

same manner two waves exist in area 1: one propagates in the normal direction and another is declined at an angle θ. The equations for the scattered electric E_1^{e} and magnetic H_1^{e} fields as well as electric E_2^{e} and magnetic H_2^{e} fields created by these electric currents in area 1 and area 2, respectively, are written as follows:

$$\begin{aligned} H_2^{\mathrm{e}} &= -H_1^{\mathrm{e}} = \frac{1}{2}\, z \times J_{\mathrm{se}} = \frac{E_{\mathrm{inc}}}{2\eta_0}\, y - \frac{E_{\mathrm{inc}}}{2\eta_0}\, \sqrt{\cos\theta}\, e^{j\phi}\, y, \\ E_2^{\mathrm{e}} &= E_1^{\mathrm{e}} = -\frac{\eta_0}{2}\, J_{\mathrm{se}} = -\frac{E_{\mathrm{inc}}}{2}\, x + \frac{E_{\mathrm{inc}}}{2}\, \frac{e^{j\phi}}{\sqrt{\cos\theta}}\, x. \end{aligned} \tag{37}$$

Likewise, for the magnetic surface current the scattered fields are shown in Figure 21.

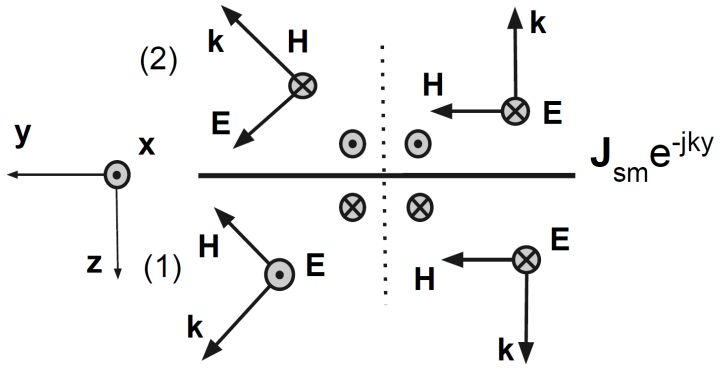

Figure 21. Scattered fields created by the magnetic surface current in both $-z$ (area 2) and $+z$ (area 1) half-spaces.

The equations for the scattered electric E_1^{m} and magnetic H_1^{m} fields in area 1 as well as the

scattered electric E_2^{m} and magnetic H_2^{m} fields in area 2 created by the magnetic currents are defined as:

$$\begin{aligned} E_2^{\mathrm{m}} = -E_1^{\mathrm{m}} &= -\frac{1}{2}\, z \times J_{\mathrm{sm}} = -\frac{E_{\mathrm{inc}}}{2}\, x - \frac{E_{\mathrm{inc}}}{2}\frac{e^{j\phi}}{\sqrt{\cos\theta}}\, x, \\ H_2^{\mathrm{m}} = H_1^{\mathrm{m}} &= -\frac{1}{2\eta_0}\, J_{\mathrm{sm}} = \frac{E_{\mathrm{inc}}}{2\eta_0}\, y + \frac{E_{\mathrm{inc}}}{2\eta_0}\sqrt{\cos\theta}\, e^{j\phi}\, y. \end{aligned} \tag{38}$$

The total fields created by the electric and magnetic surface currents are presented in Figure 22. The total scattered electric E_2 and magnetic H_2 fields created by both electric and

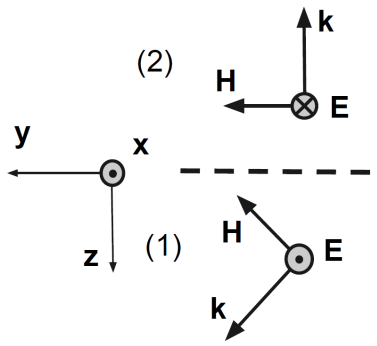

Figure 22. Total fields created by both electric and magnetic surface currents in both $-z$ (area 2) and $+z$ (area 1) half-spaces.

magnetic currents in area 2 are described as follows:

$$\begin{aligned} \sum E_2 &= -E_{\mathrm{inc}}\, x, \\ \sum H_2 &= \frac{E_{\mathrm{inc}}}{\eta_0}\, y, \end{aligned} \tag{39}$$

The total scattered electric E_1 and magnetic H_1 fields created by both electric and magnetic currents in area 1:

$$\begin{aligned} \sum E_1 &= -\frac{e^{j\phi}}{\sqrt{\cos\theta}}\, E_{\mathrm{inc}} x, \\ \sum H_1 &= \frac{E_{\mathrm{inc}}}{\eta_0}\, \sqrt{\cos\theta}\, e^{j\phi}\, y. \end{aligned} \tag{40}$$

As one can see, the electromagnetic wave behind the metamirror is cancelled and there is

an oblique reflected wave in front of the mirror. It means that the theory is correct from the beginning and the energy conservation law is satisfied on the level of fields and currents. Apparently, in the evaluation of the relations between the collective polarizabilities (response to the incident fields) and the individual polarizabilities of one single particle in free space (response to the local fields) the interactions between the particles are modelled not enough accurately, and design of an ideal lossless metasurface can be assumed to be possible. However, detailed investigations of this problem are left for future studies.

The studies described here brought up an idea of a new implementation of Huygens' principle in practice. In the next section an improvement of the metastructure based on this idea is described.

5 Huygens' principle based metamirrors

5.1 A previously considered metamirror

The idea of an ideal Huygens' metasurface is inspiring, thus, it was decided to test a metasurface design based on the direct application of this principle. As an example, a metamirror reflecting normally incident wave at an angle $\theta = 45°$ is considered (Figure 23). The metamirror consists of two types of omega particles shown in Figure 7. The parameters of the metamirror inclusions are given in Appendix 2.

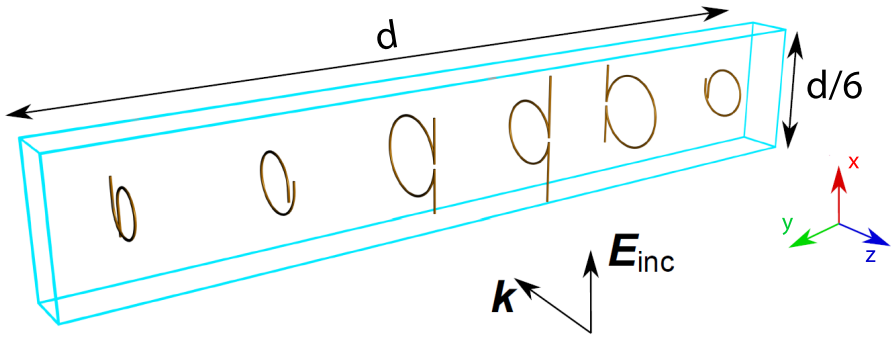

Figure 23. A model of a metamirror which reflects normally incident plane waves at an angle $\theta = 45°$. The structure consists of six sub-wavelength copper inclusions which provide a linear phase variation of reflection in the interval from 0 to $5\pi/3$ with the step of $\pi/3$.

The operating principle of the proposed metamirror is as described before. Zero transmission is achieved by the forward-scattered secondary wave which interferes with the incident wave in a destructive way. Full reflection of the normally incident wave at an chosen angle is achieved by individual adjusting of the reflection phase from each inclusion in the metamirror. A linear phase variation is provided in the metastructure to achieve the deflection of the reflected wavefront at an angle θ. The range of the phase change is from 0 to 2π with the periodicity $\lambda/\sin\theta$, where λ is the working wavelength of the metamirror. The operating frequency for the proposed structure is 5 GHz. The material of the inclusions is copper.

The model of the proposed metamirror was analyzed with Ansoft HFSS software. The model consists of 6 inclusions with the phase variations from 0 to $5\pi/3$ (step is $\pi/3$). The normally incident wave propagates along the z-axis. Figures 24a and 25a show the electric and magnetic field distributions normalized to the electric and magnetic fields of the incident wave, respectively.

The metamirror provides the reflectance of 86%. The main drawback of the structure is the uneven electric field distribution. It appears since the requirements for the linearly changing

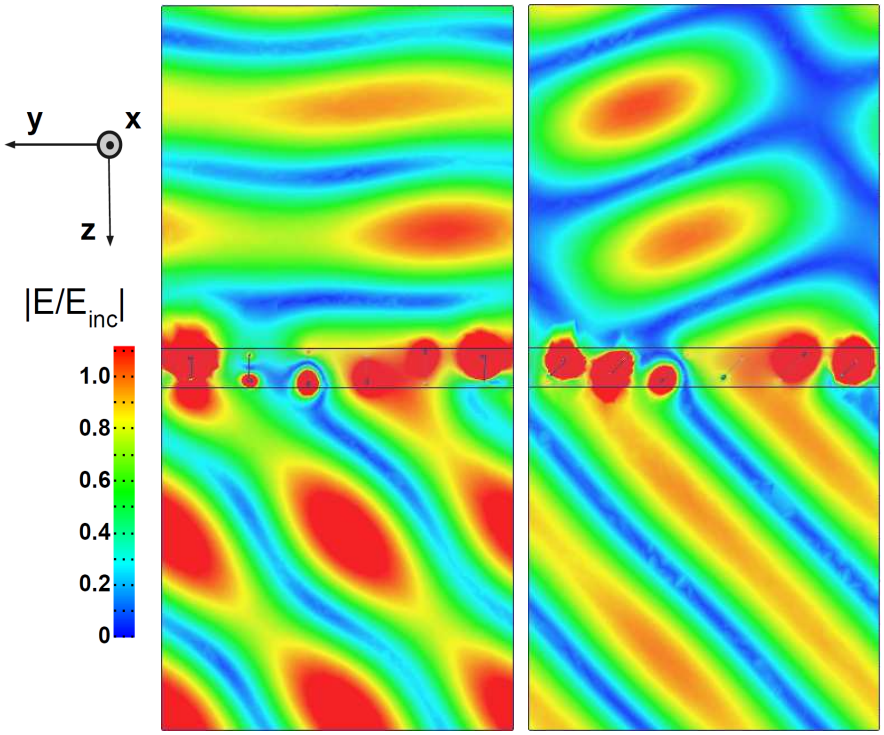

(a) (b)

Figure 24. Results of the simulations in Ansoft HFSS. The electric field distribution of the reflected (the $+z$ half-space) and transmitted (the $-z$ half-space) waves normalized to the electric field of the incident wave: (a) for the previously proposed metamirror; (b) for the Huygens' metamirror with tilted inclusions.

phase and the unity value of the amplitude are executed, but the requirements of the correct orientation of the wave vector k, the electric E and magnetic H field vectors are not fulfilled. This is the reason for a somewhat curvy wavefront in Figure 24a. To find a way to improve the performance, we suggest to use Huygens' principle design approach described in Section 4.

5.2 A metamirror with tilted omega inclusions

In order to satisfy the conditions of the tilted fields of the reflected wave (11) and (15), it was decided to tilt the omega inclusions in the array at an angle θ from the normal (Figure 26). When a normally incident wave impinges on the Huygens' metasurface, the reflected wavefront is declined at an angle θ (as it is shown in Figure 16b).

A direct attempt to optimize the tilted omega inclusion was unsuccessful because of the shape of the twisted omega particle (Figure 7a). When such a particle is declined from the normal, the influence of chirality increases. It will affect the transmission and reflection in a detri-

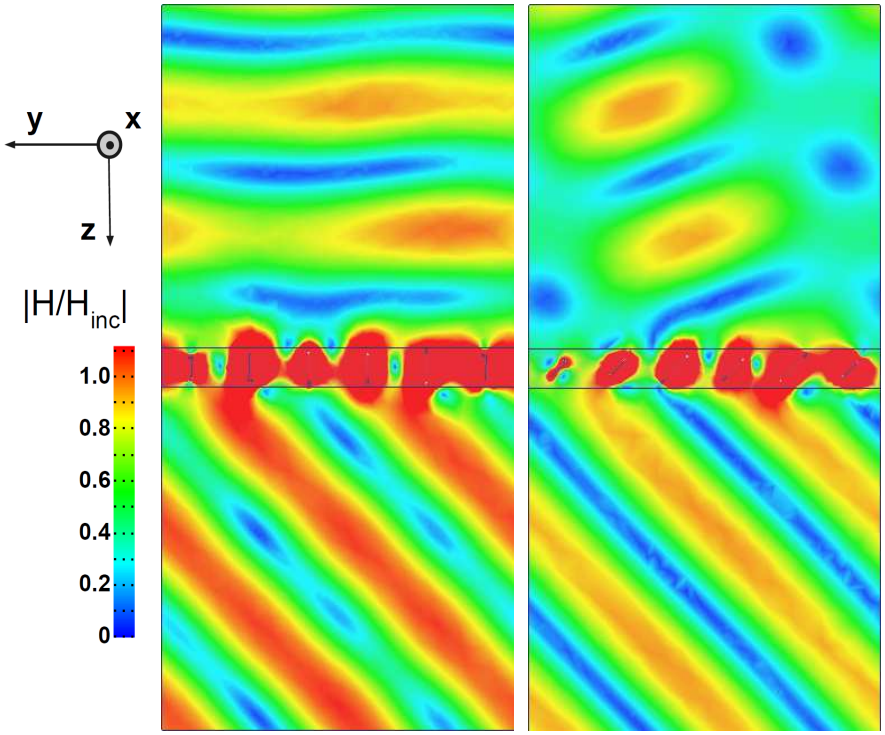

(a) (b)

Figure 25. Results of the simulations in Ansoft HFSS. The magnetic field distribution of the reflected (the $+z$ half-space) and transmitted (the $-z$ half-space) waves normalized to the magnetic field of the incident wave : (a) for the previously proposed metamirror; (b) for the Huygens' metamirror with tilted inclusions.

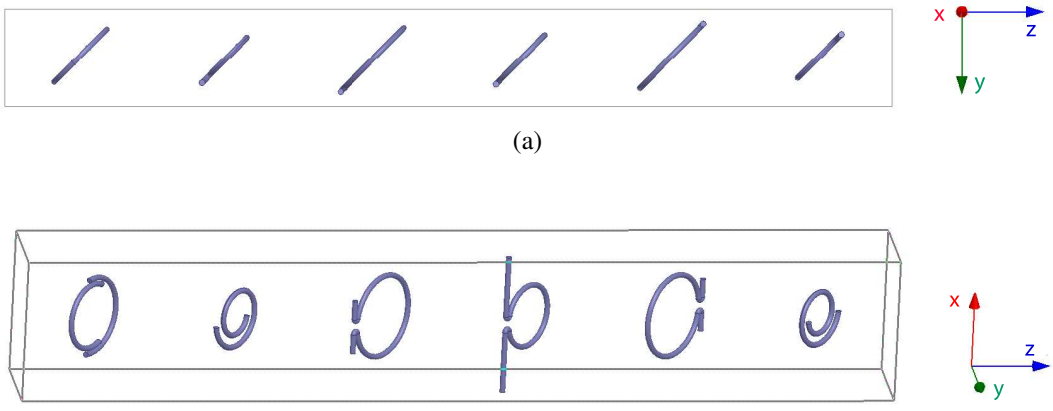

(a)

(b)

Figure 26. The metamirror with the particles tilted at $\theta = 45°$. (a) View from the top. (b) View from the side.

mental way, creating cross-polarized fields. The former is increased and the latter is reduced. The bandwidth of such a particle is extremely small what makes the structure harder to adjust. This type of omega particles was used to reach the phases 0, $\pi/3$ and $5\pi/3$. To overcome

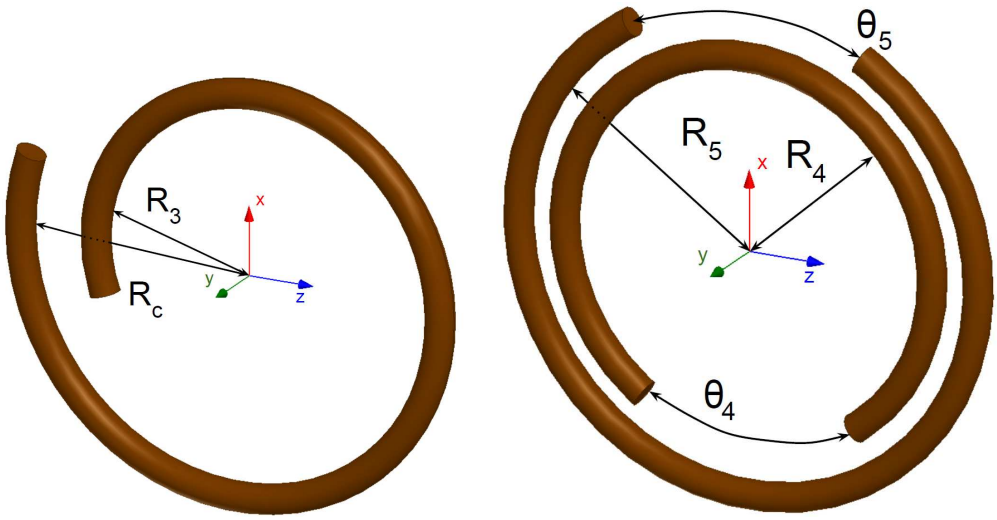

(a) (b)

Figure 27. Two different inclusions used in the metamirror. (a) Plane spiral. (b) Double SRR.

this difficulty, new inclusions were proposed instead of the twisted omega particles. With the known non-chiral particles it is hard to achieve zero phase in the tilted construction. In this work the use of double SRR was suggested (see Figure 27b). Other twisted omega particles were replaced by planar spiral particles (see Figure 27a). The parameters of the metamirror inclusions are listed in Appendix 3. The simulation results for the electric and magnetic field distributions of the reflecting metamirror with the new optimized particles are shown in Figures 24b and 25b, respectively.

The main advantage of such a structure is a nearly perfect plane wavefront in both electric and magnetic field distributions. The drawback of the structure is the decreased reflectance of 64%, which can be explained by several reasons. First of all, some part of the incident energy is transformed into cross-polarization in transmission due to the non-zero chiral effects. It is one cause of the reflectance deterioration. Another reason is variation of the interaction between the particles which behaviour model is hard to predict and adjust.

This structure gives a hope to create a perfect reflecting metamirror and will be considered in more detail in the near future.

6 Conclusions and Future Work

This thesis explores practical possibilities of realization of fully reflective thin electromagnetic structures for full control over reflected beams. The first part of the thesis studies advanced properties of previously proposed focusing metamirrors fabricated with small omega particles. Angular stability of the new mirrors was studied in detail through numerical simulations and experimentally. In the former, the focusing metamirror was illuminated by an incident wave slightly declined from the normal direction. In the latter, the opposite task was performed: a source of cylindrical waves was placed in displaced focal spots found from the simulations, and the reflected plane wave was analyzed. Both methods show remarkable results. Considering all the practical parameters of conventional mirrors such as size, weight, focal distance and manufacturing expenses, one can assert that the metamirrors possess unique properties, advantageous for many applications.

In the second part of the thesis a new concept of metamirrors based on Huygens' principle was introduced and discussed. It was shown that to construct a perfect metamirror, the requirements for a zero value of the transmitted wave amplitude, correct phase variation over the surface and correct orientation of the reflected fields E and H should be fulfilled. In previously proposed metamirrors the last of the listed requirements was not satisfied. The main idea of the new introduced concept is to create appropriate surface currents in the reflecting metastructure which satisfy all of the listed requirements. As it was shown numerically, this goal appears realistic. The only problem was faced due to not complete understanding of the metamirror design equations when the polarizabilities of the inclusions were in consideration. Despite of this issue, the concept seems to be promising. Therefore, it was decided to use it in practice. A practical realization was achieved through tilting the inclusions at a specific angle in the reflecting metastructure with a linear phase change. The new metamirror with the tilted particles was tested through numerical simulations. The advantage of the proposed structure is a nearly ideally flat wavefront in both electric and magnetic field distributions. The drawback of this particular realization is a decrease of the reflectance compared to the previously proposed metamirror.

In conclusion, in this thesis we have proved, both numerically and experimentally, that recently proposed metamirrors formed by arrays of small bianisotropic particles possess high angular stability which, in combination with their extremely small focal distances, makes them very promising for a number of applications. Furthermore, an improved design, bringing the peformance even closer to the ideal Huygens' metasurface, has been proposed and tested numerically. The analytical theory developed in this thesis proves the Huygens' surface operation at the level of the averaged surface currents and collective polarizabilities of

the unit cells. Further developments of the analytical models of particle interactions in non-uniformaly phased arrays of bianisotropic particles is needed in order to develop a complete tool for the synthesis of Huygens' metamirrors.

References

[1] The web site of the *Virtual Institute for Artificial Electromagnetic Materials and Metamaterials*. [Accessed 12.05.2015]. Available at http://www.metamorphose-vi.org.

[2] Zheludev, N. I. 2010. The road ahead for metamaterials. *Science*, vol. 328, pp. 582–583.

[3] Veselago, V. G. 1968. The electrodynamics of substances with simultaneoulsy negative values of ε and μ. *Soviet Physics Uspekhi*, vol. 10, no. 4, pp. 509–514.

[4] Veselago, V., Braginsky, L., Shklover, V. & Hafner, C. 2006. Negative refractive index materials. *Journal of Computational and Theoretical Nanoscience*, vol. 3, no. 2, pp. 1–30.

[5] Smith, D. R., Padilla, W. J., Vier, D. C., Nemat-Nasser, S. C. & Schultz, S. 2000. Composite medium with simultaneously negative permeability and permittivity. *Physical Review Letters*, vol. 84, no. 18, pp. 4184–4187.

[6] Jelinek, L. & Marques, R. 2010. Artificial magnetism and left-handed media from dielectric rings and rods. *Journal of Physics: Condensed Matter*, vol. 22, no. 2, pp. 025902.

[7] Pendry, J. B., Holden, A. J., Robbins, D. J. & Stewart, W. J. 1999. Magnetism from conductors and enhanced nonlinear phenomena. *IEEE Tansactions on Microwave Theory and Techniques*, vol. 47, no. 11, pp. 2075–2084.

[8] Serdyukov, A. N., Semchenko, I. V., Tretyakov, S. A. & Sihvola, A. 2001. Electromagnetics of Bi-anisotropic Materials: Theory and Applications. Amsterdam: Gordon and Breach Science Publishers.

[9] Asadchy, V. S., Ra'di, Y. & Tretyakov, S. A. 2014. Metamirrors [online document].[Accessed 6 May 2015]. Available as arXiv:1404.1780v1 [physics.optics].

[10] Volakis, J. 2007. Antenna Engineering Handbook, Fourth Edition. United States: McGraw-Hill Professional.

[11] Lo, Y. T. 1960. On the beam deviation factor of a parabolic reflector. *IRE Transactions on Antennas and Propagation*, vol. 8, no. 3, pp. 347–349.

[12] Encinar, J. A. 2008. Analysis, design and application of reflectarrays. VI Iberian Meeting on Computational Electromagnetics, October 22 - October 24, Chiclana, Spain.

[13] Ra'di, Y., Asadchy, V. S. & Tretyakov, S. A. 2014. Tailoring reflections from thin composite metamirrors. *IEEE Transactions on Antennas and Propagation*, vol. 62, no. 7, pp. 3749–3760.

[14] Pozar, D. M., Targonski, S. D. & Syrigos, H. D. 1997. Design of millimeter wave microstrip reflectarrays. *IEEE Transactions on Antennas and Propagation*, vol. 45, no. 2, pp. 287–296.

[15] Berry, D. J., Malech, R. G. & Kennedy, W. A. 1963. The reflectarray antenna. *IEEE Transactions on Antennas and Propagation*, vol. 11, no. 6, pp. 645–651 .

[16] Roederer, A. G. 2009. Reflectarray antennas. EuCAP 2009 - 3rd European Conference on Antennas and Propagation, March 23 - March 27, Berlin, Germany.

[17] Asadchy, V. S., Ra'di, Y., Vehmas, J. & Tretyakov, S. A. 2015. Functional metamirrors using bianisotropic elements. *Physical Review Letters*, vol. 114, no. 9, pp. 0955031–0955035.

[18] Saeidia, C. & Weide, D. 2014. Wideband plasmonic focusing metasurfaces. *Physical Review Letters* vol. 105, no. 5, pp. 0531071–0531075.

[19] Sun, S., Yang, K.-Y., Wang, C.-M., Juan, T.-K., Chen, W. T., Liao, C. Y., He, Q., Xiao, S., Kung, W.-T., Guo, G.-Y., Zhou, L. & Tsai, D. P. 2012. High-efficiency broadband anomalous reflection by gradient meta-surfaces. *Nano Letters*, vol. 12, no. 12, pp. 6223–6229.

[20] Pors, A., Nielsen, M. G., Eriksen, R. L. & Bozhevolnyi S. I. 2013. Broadband focusing flat mirrors based on plasmonic gradient metasurfaces. *Nano Letters*, vol. 13, no. 2, pp. 829–834.

[21] Pors, A. & Bozhevolnyi S. I. 2013. Plasmonic metasurfaces for efficient phase control in reflection. *Optics Express* vol. 21, no. 22, pp. 27438–27451.

[22] Farmahini-Farahani, M. & Mosallaei, H. 2013. Birefringent reflectarray metasurface for beam engineering in infrared. *Optics Letters* vol. 38, no. 4, pp. 462–464.

[23] Esfandyarpour, M., Garnett, E. C., Cui, Y., McGehee, M. D. & Brongersma, M. L. 2014. Metamaterial mirrors in optoelectronic devices. *Nature Nanotechnology* vol. 9, no. 7, pp. 542–547 .

[24] Kim, M., Wong, A. M. H. & Eleftheriades, G. V. 2014. Optical Huygens' metasurfaces with independent control of the magnitude and phase of the local reflection coefficients. *Physical Review X* vol. 4, no. 4, pp. 041042.

[25] Veysi, M., Giclu, C., Boyraz, O. & Capolino, F. 2015. Thin anisotropic metasurfaces for simultaneous light focusing and polarization manipulation. *Optical Society of America B* vol. 32, no. 2, pp. 318–323.

[26] Selvanayagam, M. & Eleftheriades, G. V. 2014. Discontinuous electromagnetic fields using orthogonal electric and magnetic currents for wavefront manipulation. *Optics Express* vol. 21, no. 12, pp. 14409–14429.

[27] Epstein, A. & Eleftheriades, G. V. 2014. Passive lossless Huygens' metasufaces for conversion of arbitrary source field to directive radiation. *IEEE Transactions on Antennas and Propagation*, vol. 62, no. 11, pp. 5680–5695.

[28] Pfeiffer, C., Emani, N. K., Shaltout, A. K., Boltasseva, A., Shalaev, V. M. & Grbic, A. 2014. Efficient light bending with isotropic metamaterial Huygens' surfaces. *Nano Letters* vol. 14, no. 5, pp. 2491–2497.

[29] Lindell, I. V. 1996. Methods for Electromagnetic Field Analysis. Piscataway, NJ: Wiley-IEEE Press.

[30] Lindell, I.V. 1996. Huygens' principle in electromagnetics. *, IEE Proceedings - Science, Measurement and Technology* vol. 143, no. 2, pp. 103–105.

[31] Balanis, C. A. 1997. Antenna Theory: Analysis and Design, 2nd Edition. New-York: Wiley.

[32] Maslovski, S. & Tretyakov, S. 2012. Perfect lensing with phase-conjugating surfaces: toward practical realization. *New Journal of Physics*, vol. 14, 035007, pp. 1–22.

Appendix 1. Parameters of the focusing metamirror inclusions.

The focusing metamirror used in the experiment consists of 23 sub-wavelength inclusions. There are two types of particles in use: twisted omega particles (Figure 7a) and Ω-shaped particles (Figure 7b). They are made of copper wire with radius 0.275 mm. The location of the inclusions is symmetrical with respect to the center of the structure. The parameters of the inclusions are represented in Table A1.1.

Table A1.1. Dimensions of the inclusions and their locations in the focusing metamirror.

Distance to the center of the metamirror, mm	Type of an inclusion	Loop radius, mm	Length of the straight wires, mm	Phase of the reflected wave, °	Position of the straight wires
0	Twisted Ω	$R_1 = 3.45$	$l_1 = 0.57$	280	-z half-space
18	Twisted Ω	$R_1 = 2.66$	$l_1 = 1.50$	306	-z half-space
33	Twisted Ω	$R_1 = 2.27$	$l_1 = 2.87$	0	-z half-space
48	Twisted Ω	$R_1 = 3.19$	$l_1 = 0.83$	65	+z half-space
63	Ω	$R_2 = 3.45$	$l_2 = 5.26$	140	+z half-space
78	Ω	$R_2 = 3.49$	$l_2 = 5.04$	218	-z half-space
93	Twisted Ω	$R_1 = 2.66$	$l_1 = 1.50$	306	-z half-space
108	Twisted Ω	$R_1 = 2.50$	$l_1 = 1.90$	27	+z half-space
123	Ω	$R_2 = 3.77$	$l_2 = 3.55$	113	+z half-space
13	Ω	$R_2 = 3.33$	$l_2 = 5.79$	207	-z half-space
153	Twisted Ω	$R_1 = 3.16$	$l_1 = 0.88$	285	-z half-space
168	Twisted Ω	$R_1 = 3.44$	$l_1 = 2.09$	19	+z half-space

Appendix 2. Parameters of the known reflecting metamirror inclusions.

The reflecting metamirror represented in [17] consists of 6 sub-wavelength inclusions. There are two types of particles in use: twisted omega particles (Figure 7a) and Ω-shaped particles (Figure 7b). They are made of copper wire with radius 0.275 mm. The parameters of the inclusions are represented in Table A2.1.

Table A2.1. Dimensions of the inclusions and their locations in the focusing metamirror.

Location along the y-axis within the period g	Type of an inclusion	Loop radius, mm	Length of the straight wires, mm	Phase of the reflected wave, $^\circ$
$-5g/12$	Twisted Ω	$R_1 = 2.79$	$l_1 = 1.29$	$5\pi/3$
$-g/4$	Ω	$R_2 = 3.43$	$l_2 = 3.49$	$4\pi/3$
$-g/12$	Ω	$R_2 = 2.88$	$l_2 = 5.42$	π
$g/12$	Ω	$R_2 = 3.35$	$l_2 = 4.01$	$2\pi/3$
$-g/4$	Twisted Ω	$R_1 = 3.01$	$l_1 = 1.00$	$\pi/3$
$-5g/12$	Twisted Ω	$R_1 = 2.28$	$l_1 = 2.87$	0

Appendix 3. Parameters of the new-created reflecting metamirror inclusions.

The reflecting metamirror described in the present work consists of 6 sub-wavelength inclusions. There are tree types of particles in use: Ω-shaped particles (Figure 7b), spiral particles (Figure 27a) and double SRR (Figure 27b). They are made of copper wire with radius 0.275 mm. The parameters of the particles are represented in Table A2.1.

Table A3.1. Dimensions of the inclusions and their locations in the focusing metamirror.

Location along the y-axis within the period g	Type of an inclusion	Loop radius, mm	Length of the straight wires, mm
$-5g/12$	Spiral	$R_3 = 1.59$	-
$-g/4$	Ω	$R_2 = 3.43$	$l_2 = 3.49$
$-g/12$	Ω	$R_2 = 2.88$	$l_2 = 5.42$
$g/12$	Ω	$R_2 = 3.35$	$l_2 = 4.01$
$-g/4$	Spiral	$R_3 = 1.60$	-
$-5g/12$	Double SRR	$R_4 = 3.22$ $R_5 = 3.82$	-

Radius change per turn, mm	Number of turns	Loop angle	Phase of the reflected wave, $^\circ$
$R_c = 1.1$	1.45	-	$5\pi/3$
-	-	-	$4\pi/3$
-	-	-	π
-	-	-	$2\pi/3$
$R_c = 1.2$	1.45	-	$\pi/3$
-	-	$\theta_4 = 115^\circ$ $\theta_5 = 110^\circ$	0